Adenomatous polyposis coli nucleates actin assembly to drive cell migration and microtubule-induced focal adhesion turnover

M. Angeles Juanes,[1] Habib Bouguenina,[2] Julian A. Eskin,[1] Richa Jaiswal,[1] Ali Badache,[2] and Bruce L. Goode[1]

[1]Department of Biology, Brandeis University, Waltham, MA
[2]Centre de Recherche en Cancérologie de Marseille, Institut National de la Santé et de la Recherche Médicale, Institut Paoli-Calmettes, Aix-Marseille Université, Centre National de la Recherche Scientifique, Marseille, France

Cell motility depends on tight coordination between the microtubule (MT) and actin cytoskeletons, but the mechanisms underlying this MT–actin cross talk have remained poorly understood. Here, we show that the tumor suppressor protein adenomatous polyposis coli (APC), which is a known MT-associated protein, directly nucleates actin assembly to promote directed cell migration. By changing only two residues in APC, we generated a separation-of-function mutant, APC (m4), that abolishes actin nucleation activity without affecting MT interactions. Expression of full-length APC carrying the m4 mutation (APC (m4)) rescued cellular defects in MT organization, MT dynamics, and mitochondrial distribution caused by depletion of endogenous APC but failed to restore cell migration. Wild-type APC and APC (m4) localized to focal adhesions (FAs), and APC (m4) was defective in promoting actin assembly at FAs to facilitate MT-induced FA turnover. These results provide the first direct evidence for APC-mediated actin assembly in vivo and establish a role for APC in coordinating MTs and actin at FAs to direct cell migration.

Introduction

Directed cell migration is essential in early animal development, tissue morphogenesis and regeneration, and in immune surveillance (Weijer, 2009; Shaw and Martin, 2016). Furthermore, defects in directed cell movement are associated with tumorigenesis and metastasis (Bravo-Cordero et al., 2012). Cell migration can be divided into four coordinated steps: (1) protrusion of the leading edge; (2) adhesion to the substrate; (3) contraction of the cell body; and (4) release/turnover of adhesions. Actin polymerization drives protrusion of the leading edge, and actomyosin contraction facilitates forward movement of the cell body. These stages of cell migration require spatially and temporally controlled assembly and disassembly of integrin-based focal adhesions (FAs), which link the actin cytoskeleton to the ECM (Ridley et al., 2003). New FAs are continuously formed at the leading edge as smaller nascent adhesions, only some of which mature into larger FAs, and these are subsequently disassembled near the cell body and trailing edge. Pioneering live-imaging experiments from Kaverina and colleagues showed that microtubules (MTs) grow along stress fibers to contact FAs, where they are transiently captured, triggering FA disassembly (Kaverina et al., 1998, 1999; Small et al., 2002; Efimov et al., 2008). The spectraplakin ACF7/MACF, which has separate binding domains for actin and MTs, facilitates MT growth along stress fibers (Wu et al., 2008; Yue et al., 2016). How MT plus ends are captured at FAs is still not well understood, but appears to involve KANK–Talin interactions (Bouchet et al., 2016). It is also not yet clear how MT capture leads to FA disassembly, but available evidence suggests that this involves clathrin-mediated endocytosis, NBR1-mediated autophagy, and delivery of exocytic vesicles carrying matrix metalloproteases (MMPs) that sever integrin–ECM connections (Ezratty et al., 2005, 2009; Stehbens et al., 2014; Kenific et al., 2016).

Another suggested mediator of MT–actin cross talk is adenomatous polyposis coli (APC), which interacts directly with both MTs and actin filaments (Munemitsu et al., 1994; Moseley et al., 2007). *APC* is the "gatekeeper" gene in human colorectal tumorigenesis, with autosomal-dominant C-terminal truncations of APC leading to >80% of all colorectal cancers (Kinzler et al., 1991; Näthke, 2004; Akiyama and Kawasaki, 2006; Kwong and Dove, 2009). APC is also critical for directed cell migration and for cell and tissue morphogenesis (Sansom et al., 2004; Kroboth et al., 2007; McCartney and Näthke, 2008; Matsumoto et al., 2010; Zaoui et al., 2010). APC is a large (310 kD) multidomain protein with many in vivo binding partners (Fig. 1, A and B) and has functions in both Wnt signaling and

Correspondence to Bruce L. Goode: goode@brandeis.edu; M. Angeles Juanes: juanes@brandeis.edu

Abbreviations used: APC, adenomatous polyposis coli; CC, coiled coil; FA, focal adhesion; FL-APC, full-length APC; FOV, field of view; MT, microtubule; Ni-NTA, nickel–nitrilotriacetic acid; OG, Oregon green; RMA, rabbit skeletal muscle actin; si-APC, silenced APC; TIRF, total internal reflection fluorescence.

The Rockefeller University Press
J. Cell Biol. Vol. 216 No. 9 2859–2875
https://doi.org/10.1083/jcb.201702007

cytoskeletal regulation (Näthke, 2005; Barth et al., 2008; McCartney and Näthke, 2008). The N terminus of APC (residues 1–958) harbors three separate self-association domains and an Armadillo repeat region that interacts with kinesin-2, IQGAP, APC-stimulated guanine nucleotide exchange factor, and other cytoskeletal regulatory proteins. The central region of APC (residues 959–2,129) binds Axin and β-catenin and regulates β-catenin degradation to control downstream gene expression. The C terminus of APC (residues 2,130–2,843) binds to MTs, the kinesin-1 mitochondrial adapters Miro and Milton, and the MT plus end–tracking protein EB1 and functions primarily in cytoskeletal regulation (Nelson and Näthke, 2013; Ruane et al., 2016). In vivo, APC decorates MTs and is transported toward their plus ends by kinesin-1 and -2 (Mimori-Kiyosue et al., 2000). APC also localizes to actin-rich cortical regions in cells. This APC localization is independent of MTs, but depends in part on APC interactions with IQGAP1 (Näthke et al., 1996; Rosin-Arbesfeld et al., 2001; Mogensen et al., 2002; Watanabe et al., 2004; Langford et al., 2006a,b). The C-terminal region of APC, consisting of its Basic domain and EB1-binding site, is required for proper MT organization and dynamics in cells and is required for directed cell migration and mitochondrial distribution (Sansom et al., 2004; Kroboth et al., 2007; Mills et al., 2016). These cellular functions have been attributed to APC's interactions with MTs. However, the APC Basic domain (APC-B; 2,167–2,674) also binds to actin with high affinity and potently stimulates actin nucleation in vitro, both alone and synergistically with formins (Moseley et al., 2007; Okada et al., 2010; Breitsprecher et al., 2012). Furthermore, a C-terminal fragment of the *Drosophila melanogaster* homologue of APC, APC1, directly stimulates actin polymerization in vitro, and *Drosophila* APC2 plays a critical role in vivo in the assembly of actin structures (Webb et al., 2009; Jaiswal et al., 2013b).

Until now, the lack of clean separation-of-function mutants of APC has made it challenging to disentangle APC's effects on actin versus MTs and thereby assess the in vivo importance of its different interactions and activities. Here, we have generated a specific separation-of-function mutant for APC by changing only two residues and show that this mutant abolishes APC's actin nucleation effects without altering APC's interactions with MTs or in vivo functions in MT organization and dynamics. Using this mutant, we show that APC promotes actin assembly at FAs and that its actin nucleation activity is required for MT-induced FA turnover and directed cell migration.

Results

Generation of an actin nucleation-impaired mutant of APC

With the goal of generating a mutant of APC impaired specifically in actin nucleation, we first mapped the nucleation activity using truncation analysis (Fig. S1 A). Previously, we had shown that APC-B (2,167–2,674) and APC-C (2,130–2,843) are indistinguishable in their abilities to bind actin monomers with high affinity, dimerize, nucleate actin assembly, and directly collaborate with the formin Dia1 to assemble actin filaments via a "rocket launcher" mechanism (Moseley et al., 2007; Okada et al., 2010; Breitsprecher et al., 2012). Two sequences in APC-B were required for actin nucleation in vitro: actin nucleation sequences 1 and 2 (ANS1 and ANS2; Okada et al., 2010). Because MT binding was mapped to a region overlapping with ANS1, here we focused on dissecting ANS2, reasoning that mutations in this region would be more likely to uncouple actin nucleation from MT binding.

We purified C-terminal truncations in ANS2 (Fig. S1 A) to compare their abilities to promote actin assembly in total internal reflection fluorescence (TIRF) microscopy assays (Fig. S1 B) and bulk pyrene-actin assembly assays (Fig. S1 C). Using these approaches, we identified a 17–amino acid sequence in ANS2 (2,526–2,542) required for actin nucleation that is highly conserved across vertebrate species (Fig. S1 D). We then introduced point mutations into this sequence in the context of intact APC-B and purified the four mutant APC-B polypeptides (m1–m4), each carrying two to four alanine substitutions (Fig. 1 A). One mutant, m4 (L2539A and I2541A), failed to promote actin nucleation, whereas the other three mutants had activities similar to APC-B (WT) (Fig. 1, C–E; and Video 1). APC-B (m4) also failed to collaborate in vitro with the formin Daam1 (Fig. 1, F and G) and the formin mDia1 (Fig. S1 E) in promoting actin assembly in the presence of capping protein and profilin. However, APC-B (m4) was indistinguishable from APC-B (WT) in binding to F-actin and MTs in cosedimentation assays and in bundling F-actin and MTs in low-speed pelleting assays (Fig. S2, A–E). Thus, the m4 mutant is impaired specifically in actin nucleation.

To better understand how the m4 mutant disrupts actin nucleation, we compared APC-C (WT) and mutant APC-C (m4) polypeptides for G-actin binding and dimerization, the two known requirements for APC-mediated actin nucleation (Okada et al., 2010). In single-molecule TIRF colocalization experiments, fluorescently labeled APC-C molecules (WT and m4) were passively adsorbed to the viewing surface. Both WT and the m4 mutant recruited soluble, fluorescently labeled actin monomers (Fig. 1 H and Fig. S2 F). Furthermore, the WT and m4 polypeptides were indistinguishable in actin monomer binding over a wide range of concentrations in fluorescence-based binding assays (Fig. 1 I). In contrast, an N-terminally truncated APC-B protein (*ΔN6*; *2,392–2,674*) failed to bind G-actin (Fig. 1 I) or to nucleate actin assembly (Fig. S2 G), demonstrating that the actin monomer binding interactions of the WT and m4 polypeptides are specific.

To assess the oligomerization states of the WT and m4 polypeptides, we performed single-molecule step photobleaching (Fig. 1, J and K). SNAP-649–APC-C (WT) molecules were predominantly dimers, consistent with previous hydrodynamic and step photobleaching analyses (Okada et al., 2010; Breitsprecher et al., 2012). In contrast, SNAP-649–APC-C (m4) molecules were primarily monomeric, indicating that the m4 point mutations weaken dimerization. It was previously shown that APC-B dimers bind to the C-terminal tails of formin dimers (Breitsprecher et al., 2012), suggesting a multivalent interaction that may be weakened by the m4 mutant. Indeed, APC-B (m4) showed reduced binding to the formin Daam1 (Fig. S2 H). Importantly, full-length APC (FL-APC) molecules carrying the m4 mutations are predicted to dimerize because of the presence of at least three other dimerization domains N-terminal to the Basic domain (Fig. 1 B; Joslyn et al., 1993; Su et al., 1993; Li et al., 2008; Kunttas-Tatli et al., 2014). As such, APC architecture may be similar to full-length formins, which have at least two distinct domains maintaining dimerization (Breitsprecher and Goode, 2013). Given this architecture (Fig. 1 B), we asked whether fusing the N-terminal dimerization (coiled coil [CC]) domain of APC to the Basic domain could restore

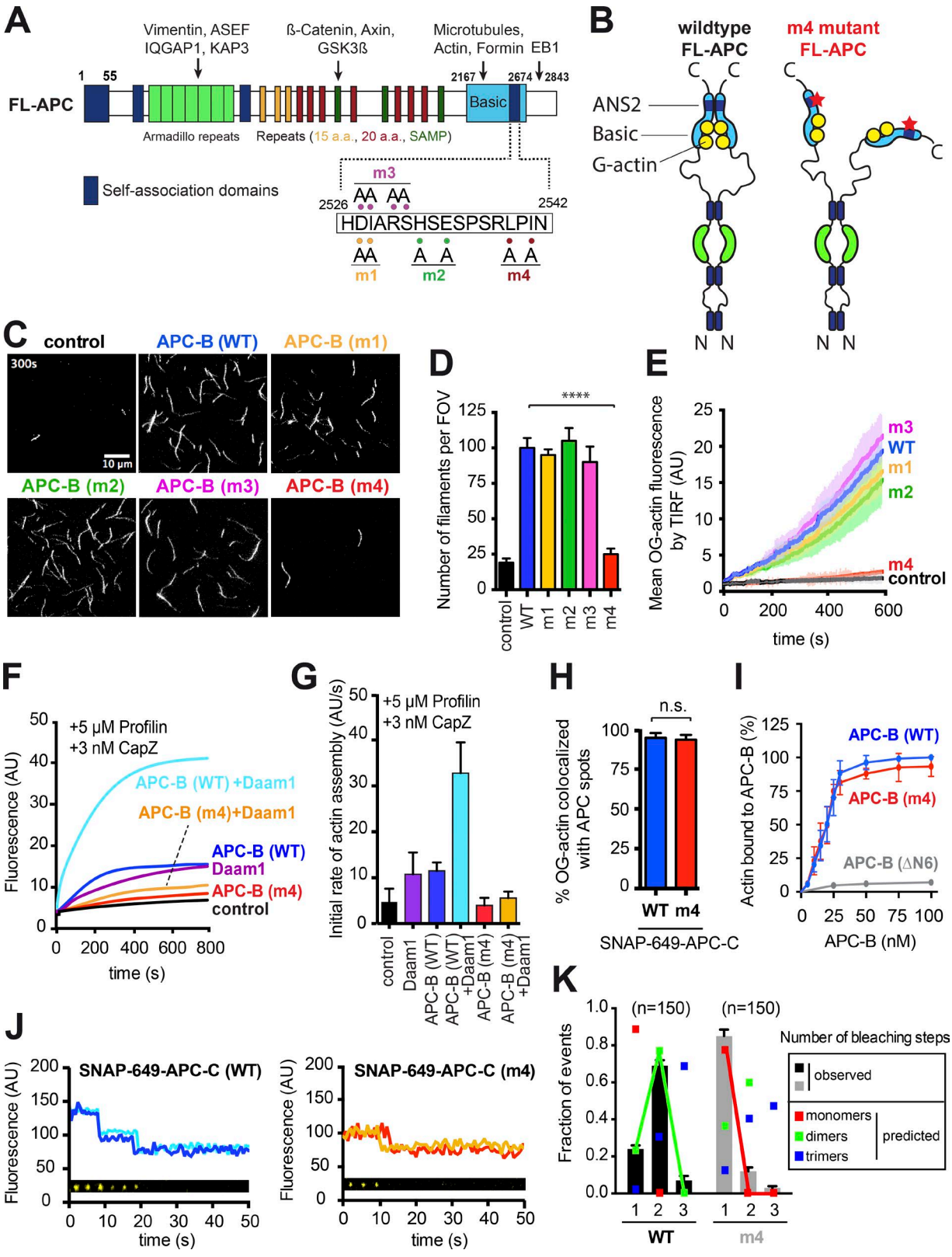

Figure 1. **Specific point mutations in the APC Basic domain disrupt actin nucleation.** (A) Schematic of FL-APC domains and their interactions. Highlighted below the schematic is the 17–amino acid sequence (2,526–2,542) identified as required for actin nucleation (Fig. S1) and the four alanine substitution mutants that were generated (m1–m4). (B) Cartoon of WT and m4 FL-APC molecules as dimers, color coded as in A and with G-actin in yellow and sites of m4 mutations indicated by red stars. (C) Representative images from TIRF assays 300 s after initiation of actin assembly. Reactions contain 1 µM G-actin (10% OG labeled and 0.2% biotin labeled) and 5 µM profilin, with or without 5 nM APC-B (WT or mutant). (D) Mean number of actin filaments assembled per FOV in TIRF assays as in B. Data averaged from three FOVs in each of three independent experiments (n = 200 actin filaments per condition). Ordinary one-way Student's t test, Dunnett's multiple comparisons test. (E) Quantification of OG-actin fluorescence intensity over time in TIRF assays; conditions as in

actin nucleation activity to the m4 mutant (Joslyn et al., 1993; Su et al., 1993). The resulting CC-APC-B (m4) polypeptide, however, failed to stimulate actin nucleation, in contrast to the CC-APC-B (WT) polypeptide (Fig. S2, I and J). From these results, we conclude that dimerization specifically in the ANS2 of the Basic domain is required for nucleation, possibly by bringing into close proximity actin monomers bound by each half of the dimer (Fig. 1 B).

Expression of FL-APC (m4) mutant in cells leads to reduced levels of F-actin and defects in directed cell migration

To test the efficacy of the APC (m4) mutant as a separation-of-function mutant in vivo, we first examined its effects on cellular actin and on MT organization and dynamics. Endogenous APC was depleted from U2OS human osteosarcoma cells using siRNAs and was confirmed on Western blots and by immunofluorescence (Fig. 2, A and B; and Fig. S3 A). Cells were also transfected with rescue constructs expressing RNAi-refractive untagged FL-APC (WT or m4). Western blot and immunofluorescence experiments showed that transfected FL-APC (WT) and FL-APC (m4) were expressed at similar levels as endogenous APC (Fig. 2, A and B; and Fig. S3 A), suggesting that APC expression in cells may be autoregulated. Silencing APC led to a significant reduction in F-actin density (fluorescence intensity per area) in cells, and these defects were rescued by expression of FL-APC (WT) but not FL-APC (m4) (Fig. 2, C and D). APC silencing also caused a dramatic reduction in MT density at the cell periphery, consistent with a previous study (Zaoui et al., 2010). However, expression of either FL-APC (WT) or FL-APC (m4) rescued the defects (Fig. 2, E and F). APC silencing also altered the mean MT growth rate, lifetime, and dynamicity, measured by quantitative tracking of GFP-EB1 comets (Fig. 2, G and H; Fig. S3 B; and Video 2), and these defects were rescued by expression of WT or m4 FL-APC. Finally, APC silencing led to a dramatic redistribution of mitochondria from the plasma membrane to the perinuclear zone, which depends on APC Basic domain interactions with the kinesin-1 adapters Miro and Milton (Mills et al., 2016). Once again, these defects were rescued by expression of WT or m4 FL-APC (Fig. 2, I and J). Together, these results demonstrate that expression of FL-APC (m4) specifically reduces F-actin levels in cells while fully restoring APC functions in MT organization, MT dynamics, and mitochondrial distribution.

Next, we examined the effects of FL-APC (m4) on directed cell migration, which requires tight coordination between the MT and actin cytoskeletons (Rodriguez et al., 2003). We first compared the migration of U2OS cells in wound-healing assays after APC silencing and rescue (Fig. 3, A and B). Initial wound sizes varied slightly, but experiments were repeated 18 times for each condition, and mean wound sizes were not significantly different (Fig. 3 C). Silencing of APC severely compromised wound healing (Fig. 3, A and B; and Video 3), and these defects were rescued by expression of FL-APC (WT) but not FL-APC (m4) (Fig. 3 B). In addition, we analyzed the migration trajectories of individual cells at the edge of wounds (representative traces; Fig. 3 D) and quantified directional persistence, expressed as the ratio of the length to distance (L/D; Fig. 3 E). Control cells had migration paths with L/D ratios close to one, indicative of straight, directional migration. APC silencing caused severe defects in the directionality of migration, and these defects were rescued by expression of FL-APC (WT) but not FL-APC (m4). Similar defects were observed in wound-healing assays when FL-APC (m4) was expressed over endogenous APC (i.e., without silencing; Fig. S3, C–E; and Video 4). Thus, FL-APC (m4) effects appear to be dominant. This is possibly caused by full-length mutant molecules dimerizing with WT molecules, similar to C-terminally truncated APC dimerizing with full-length WT APC to cause colon cancer (Fig. 1 B; Kinzler et al., 1991). In addition, we tested the effects of the FL-APC (m4) mutant on individual MDA-MB-231 breast carcinoma cells migrating toward a chemoattractant gradient in Dunn chambers. We monitored at least 150 cells per condition and found that control cells migrated in a polarized manner toward the gradient, which was quantified in rose plots of the migration paths (Fig. 3 F) and by the Y forward migration index (Fig. 3 G). Depletion of APC caused random migration, and FL-APC (WT) rescued these defects, whereas FL-APC (m4) was unable to restore directional migration (Fig. 3, F and G; and Video 5). Together, these results suggest that APC-mediated actin nucleation is required for the directed migration of individual cells and sheets of cells.

Expression of FL-APC (m4) mutant results in severe defects in FA turnover

Because APC was previously localized to FAs and directed cell migration depends on MT–actin cross talk at FAs (Matsumoto et al., 2010), we investigated the potential role of APC-mediated actin nucleation in FA dynamics. We first used live TIRF imaging to examine localization of GFP-tagged FL-APC in U2OS cells and found that GFP–FL-APC (WT and m4) tightly colocalized with mCherry-Zyxin, a marker of mature FAs (Fig. 4 A). GFP–FL-APC (WT and m4) were expressed at levels similar to endogenous APC (Fig. 4 B). In addition, GFP–FL-APC (WT) rescued silenced APC (si-APC) defects in wound-healing assays (Fig. S3 F), demonstrating that the GFP tag does not compromise function.

We examined the effects of APC silencing and rescue on levels of two key FA markers, Paxillin phosphorylated at Tyr118 (P-Paxillin) and activated FAK phosphorylated at Tyr397 (FAK-pY397). Phosphorylation of each of these components is reduced when FA turnover is impaired (Webb et al., 2002; Ezratty et al., 2005, 2009; Zaidel-Bar et al., 2007). APC silencing reduced cellular levels of P-Paxillin and FAK-pY397 on West-

B. Data averaged from fluorescence intensity in ≥3 FOVs. ****, $P < 0.0001$ (F) Bulk actin assembly assays containing 2 µM G-actin (5% pyrene labeled), 5 µM profilin, 3 nM capping protein, and 10 nM APC-B (WT or m4) and/or 1 nM C-Daam1. (G) Initial rates of actin assembly from bulk assays as in E, averaged from three independent experiments. (H) Quantification of single-molecule TIRF colocalization of surface-adsorbed SNAP-649–APC-C (WT or m4) with soluble, Latrunculin B–bound OG-labeled actin monomers. Data averaged from three independent experiments ($n \geq 215$ spots per condition). Two-tailed Student's *t* test. (I) Fluorescence assay measuring binding of APC-B (WT, m4, and ΔN6; 0–100 nM) to 100 nM Latrunculin B–bound pyrene-labeled actin monomers. (J) Representative step photobleaching of single molecules of SNAP-649–APC-C (WT and m4). Insets show raw images corresponding to the traces. (K) Distribution of number of observed bleaching events for SNAP-649–APC-C (WT) and SNAP-649–APC-C (m4) single molecules, and comparison to predicted number of bleaching events (based on calculated SNAP-649 labeling efficiency; Breitsprecher et al., 2012) for different oligomeric states (color-coded squares). Lines connect squares for the best fit to the observed data. n.s., not significant. Error bars, SD.

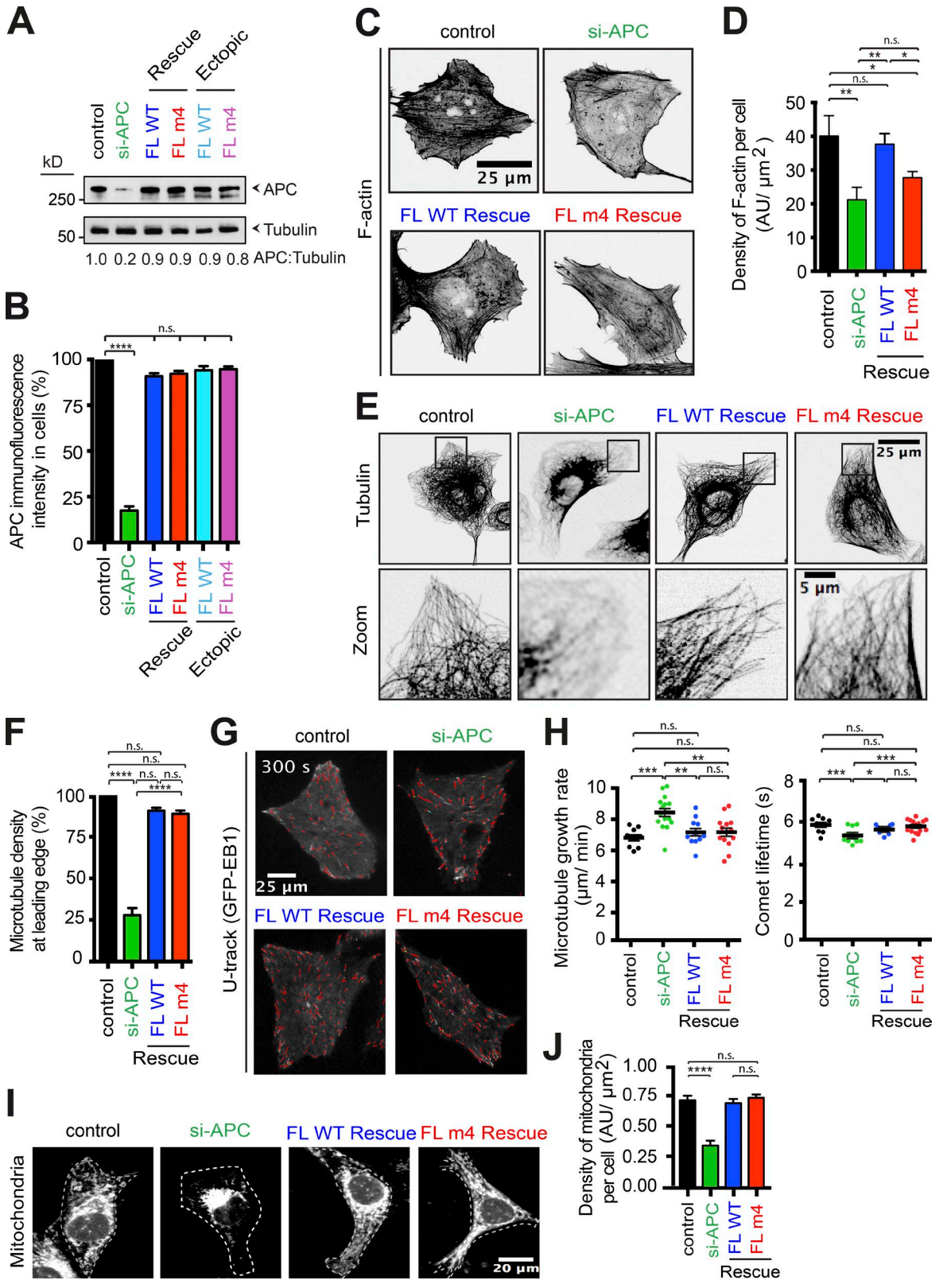

Figure 2. **Expression of mutant (m4) FL-APC leads to reduced F-actin levels in cells without altering MT organization and dynamics or mitochondria distribution.** (A) Western blots of whole cell extracts from mock-treated (control) U2OS cells, cells depleted of endogenous APC (si-APC), depleted cells rescued by plasmids expressing si-resistant untagged FL-APC (WT or m4), and cells ectopically expressing untagged FL-APC (WT or m4) probed with APC and tubulin (loading control) antibodies. Below each lane of the blot is the ratio of APC to tubulin relative to control cells. (B) Quantification of APC signal in cells measured by immunofluorescence intensity (n = 30 cells per condition; Fig. S3) and normalized to cell area from cells treated as in A. Data averaged from three or more experiments. Error bars, SD; two-tailed Student's t test. (C) Representative images showing F-actin organization (rhodamine-phalloidin staining) in mock-treated (control) U2OS cells, cells depleted of endogenous APC (si-APC), and depleted cells rescued by plasmids expressing si-resistant

ern blots (Fig. 4 C and Fig. S3 F), as reported by Matsumoto et al. (2010). These levels were restored by FL-APC (WT) but not FL-APC (m4). Similar results were obtained when FL-APC (WT and m4) were ectopically expressed over endogenous APC (Fig. 4 C), again indicating that m4 mutant effects are dominant. Ectopic expression was used for all subsequent analyses of FA turnover, simplifying procedures and producing healthier cells. By immunofluorescence, we observed a decrease in P-Paxillin staining in the numerous small foci seen in control cells and an increase in P-Paxillin staining in the larger, less abundant FAs (Fig. 4 D). Moreover, these defects correlated with an increase in the area of individual FAs (Fig. 4 E) and a decrease in the number of FAs per cell (Fig. 4 F). Similar results were obtained using antibodies to another FA marker, vinculin (Fig. S3 G; Webb et al., 2002; Ezratty et al., 2005, 2009; Zaidel-Bar et al., 2007). Collectively, these results show that even though mutant FL-APC (m4) localizes to FAs, it fails to support FA turnover, indicating that APC-mediated actin assembly is required.

We also tested whether expression of FL-APC (m4) affected the ability of MTs to reach FAs and subsequently trigger their disassembly (Kaverina et al., 1998; Krylyshkina et al., 2002; Small et al., 2002; Stehbens and Wittmann, 2012). APC silencing led to a striking loss of MT staining at FA-enriched cortical regions, but MTs were normal in cells expressing FL-APC (WT) or FL-APC (m4) (Fig. 4 G). This suggests that the FA turnover defects caused by FL-APC (m4) are not caused by MTs failing to reach FAs. Because FAs translocate from the periphery toward the center of cells (Smilenov et al., 1999), we also used live TIRF imaging in U2OS cells to examine how GFP-Paxillin translocation was affected by expression of FL-APC (m4). FAs translocated normally in control cells, as indicated by the minimal overlap in overlays of FA staining from 0- and 20-min time points (Fig. 4, H and I). APC silencing led to a striking disruption of FA translocation, as indicated by strong overlap between the 0- and 20-min signals. In addition, these defects were rescued by expression of FL-APC (WT) but not FL-APC (m4). These results suggest that proper FA translocation and turnover requires APC-mediated actin assembly.

To directly test how FL-APC (m4) expression affects MT-induced FA disassembly, we used an assay in which cells are treated with nocodazole to depolymerize MTs under starvation conditions. Then, nocodazole was washed out to allow MTs to regrow and induce FA disassembly (Ezratty et al., 2005, 2009; Chao and Kunz, 2009; Chao et al., 2010). In control cells, FAs increased in intensity after nocodazole treatment, as previously shown (Bershadsky et al., 1996; Kirchner et al., 2003), and by 30–60 min after washout of nocodazole, MTs regrew and FAs were disassembled (Fig. 5, A and B). By 120 min, new FAs began to appear as less intense spots. In stark contrast, si-APC cells and cells expressing FL-APC (m4) regrew MTs but failed to disassemble FAs. In si-APC cells, peripheral MT staining also was diminished, as expected (Fig. 2), and MT staining was normal in FL-APC (m4)–expressing cells. Thus, the observed FA turnover defects cannot be attributed to impaired MT growth.

Additionally, we monitored P-Paxillin levels by immunoblotting (Fig. 5 C). Before nocodazole treatment, P-Paxillin levels were decreased in si-APC cells and cells expressing FL-APC (m4) (Fig. 5 C), consistent with immunoblotting in Fig. 4 C. After nocodazole treatment, P-Paxillin levels increased, as expected, as a result of the loss of MT-induced FA disassembly and were similar for all conditions (Fig. 5, B and C; compare levels at t = 0). Upon nocodazole washout, P-Paxillin and FAK-pY397 levels decreased over time in control cells and FL-APC (WT) rescue cells but remained high in si-APC cells and cells expressing FL-APC (m4). It is important to note that in these experiments, total Paxillin levels remained constant, indicating that even when MTs regrew after nocodazole washout, they failed to induce FA disassembly in cells expressing FL-APC (m4). Finally, we examined the effects of FL-APC (m4) expression on F-actin levels at FAs in nocodazole-treated cells. In si-APC cells and cells expressing FL-APC (m4), F-actin staining at FAs was markedly reduced (Fig. 5, D and E). These results suggest that independent of a possible role for APC in linking MTs to FAs, APC-mediated actin assembly at FAs is instrumental to their turnover.

Discussion

In this study, we have generated what is to our knowledge the first separation-of-function mutant in APC. This tool has allowed us to rigorously test the in vivo importance of APC's actin assembly–promoting activity, which until now has only been observed in vitro (Okada et al., 2010; Breitsprecher et al., 2012; Jaiswal et al., 2013b). APC is a large protein (310 kD) with multiple domains, binding partners, and functional activities, and in vivo experiments using C-terminal truncations of APC have been difficult to interpret because they simultaneously disrupt many different interactions and activities. Our FL-APC (m4) mutant changes only two residues and abolishes APC-mediated actin assembly (alone or collaboratively with formins) without affecting APC interactions with F-actin or MTs, APC in vivo functions in MT organization and dynamics, or mitochondrial distribution. Our results show that expression of FL-APC (m4) leads to reduced F-actin levels at FAs and severe defects in FA turnover and directed cell migration. This provides the most compelling evidence to date for the importance of vertebrate APC's actin assembly–promoting activity in cells. In *Drosophila*, APC2 performs critical functions in vivo as an actin

FL-APC (WT or m4). (D) Quantification of mean F-actin density in cells. Data averaged from three independent experiments (n = 60 cells per condition). (E) Representative images showing MT organization (tubulin immunostaining) in mock-treated (control) U2OS cells, cells depleted of endogenous APC (si-APC), and depleted cells rescued by plasmids expressing si-resistant FL-APC (WT or m4). Magnifications are shown for boxed regions. (F) Quantification of MT density at cell periphery normalized to control cells (100%). Data are mean from three independent experiments (n = 50 cells per condition). (D and F) Error bars, SEM; one-way ANOVA Holm-Sidak's multiple comparison t test. (G) Representative images of GFP-EB1 comets (red) tracked in live cells as in A using TIRF microscopy and analyzed with U-track. Longer red lines reflect faster GFP-EB1 movements. (H) Quantitative analysis of GFP-EB1 comet velocities and lifetimes measured using U-track. Each data point graphed is the mean of ≥3,000 comets tracked during a 5-min observation window in a single cell (n = 10 cells per condition). Error bars, SEM; one-way ANOVA Bonferroni multiple comparison correction test. (I) Representative images of U2OS cells treated as in C and stained with MitoTracker green FM dye. (J) Quantification of mitochondrial dispersal in cells expressed as a ratio of the area of mitochondrial staining to whole cell area. Data averaged from three independent experiments (n = 30 cells per condition). Error bars, SD; one-way ANOVA Bonferroni multiple comparison correction test. Statistical differences: *, P < 0.05; **, P < 0.01; ***, P < 0.001; ****, P < 0.0001; n.s., not significant.

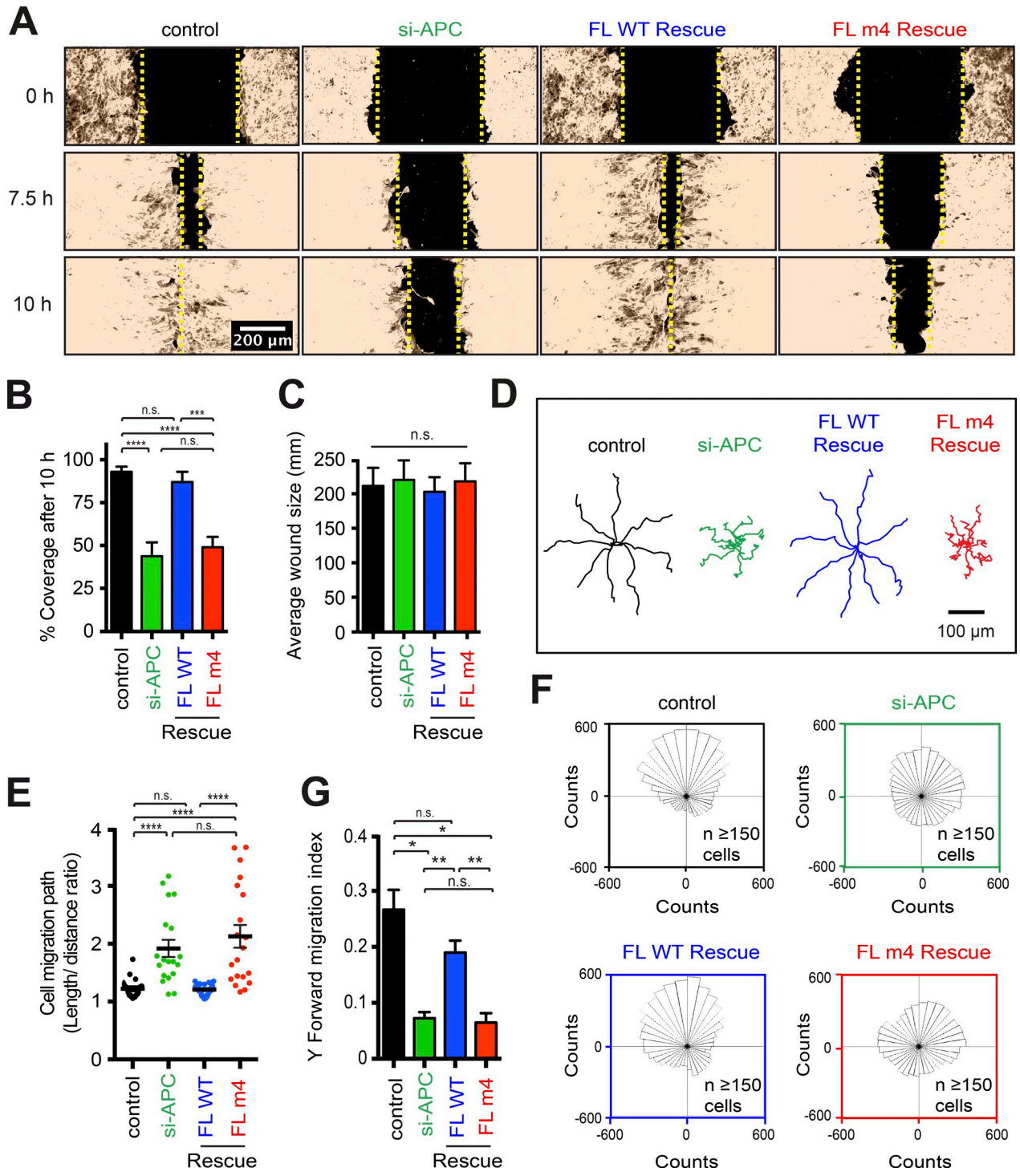

Figure 3. **Expression of mutant (m4) FL-APC causes severe defects in directed cell migration.** (A) Representative wound-healing assays showing U2OS cells stained with SiR-actin, comparing mock-treated (control) cells, cells depleted of endogenous APC (si-APC), and depleted cells rescued by plasmids expressing si-resistant FL-APC (WT or m4). Cells are shown 0, 7.5, and 10 h after scratch. Yellow dashed lines mark wound edges. (B) Quantification of wound closure 10 h after scratch, as in A. Data averaged from six independent experiments performed in triplicate. Error bars, SD; one-way ANOVA Holm-Sidak's multiple comparison test. (C) Quantification of mean wound size at t = 0. Data averaged from six independent experiments performed in triplicate. Error bars, SD; one-way ANOVA Holm-Sidak's multiple comparison test. (D) Representative traces of the migration paths of individual U2OS cells (expressing GFP-actin) moving into a wound site, displayed in radial arrays, where the center of each array is the starting point in the migration path. Shown are 8 out of the 20 traces used for quantification in E. (E) Tortuosity index of the migration paths of individual cells from C, defined as the length of the path divided by the net distance migrated (L/D; *n* = 20 cells). Error bars, SEM; two-tailed Student's *t* test. (F) Rose diagrams showing the migration angles of MDA-MB-231 cells in Dunn chamber chemotaxis assays, comparing mock-treated cells (control), cells depleted of endogenous APC (si-APC), and depleted cells rescued by plasmids expressing si-resistant FL-APC (WT or m4). Plots show data pooled from three independent experiments. (G) Y forward migration index for the same cells as in E. Error bars, SEM; two-tailed Student's *t* test. Significant differences: *, P < 0.05; **, P < 0.01; ***, P < .001; ****, P < 0.0001; n.s., not significant.

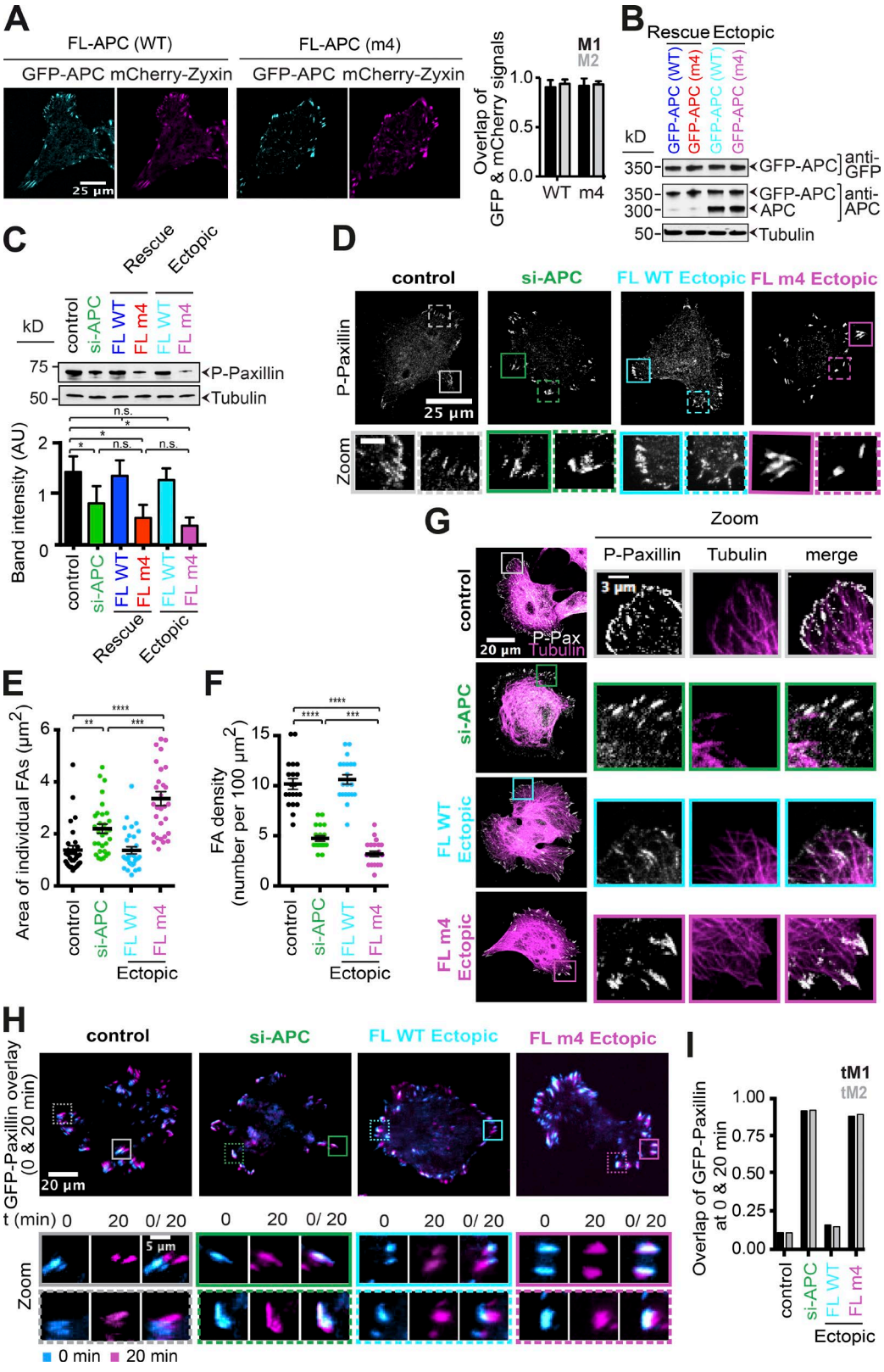

Figure 4. **Expression of mutant (m4) FL-APC disrupts FA turnover.** (A) Representative images showing GFP–FL-APC (WT and m4) colocalization with mCherry-Zyxin in U2OS cell. Graph on the right shows Mander's correlation coefficient (M1 and M2) value of overlap between GFP-APC and mCherry-Zyxin signals (n = 35 cells per condition). (B) Western blots of whole cell extracts from U2OS cells depleted of endogenous APC (si-APC) and rescued by plasmids expressing si-resistant GFP-tagged FL-APC (WT or m4), and cells ectopically expressing GFP-tagged FL-APC (WT or m4) probed with antibodies to GFP, APC, and tubulin (loading control). (C) Western blot analysis of phospho-Paxillin and tubulin (loading control) levels. Lysates are from mock-treated (control) U2OS cells, cells depleted of endogenous APC (si-APC), depleted cells rescued by plasmids expressing si-resistant FL-APC constructs (rescue FL-WT and FL-m4), and nondepleted cells expressing FL-APC constructs (ectopic FL-WT and FL-m4). Data averaged from three separate blots. Error bars, SD; two-

regulator (Webb et al., 2009; Zhou et al., 2011). The in vivo actin functions of *Drosophila* APC1, the closer homologue of human APC, are not as well defined. However, the Basic domain of *Drosophila* APC1, like that of human APC, nucleates actin assembly in vitro (Jaiswal et al., 2013b), suggesting that this function is conserved.

Our results have uncovered a new role for APC at FAs, both in stimulating actin assembly and in facilitating MT-induced FA turnover. MTs grow along actin stress fibers to reach FAs, where they are transiently captured, and then undergo catastrophe and shrink back. They subsequently recover and return to FAs in repeated cycles to induce FA disassembly (Kaverina et al., 1998, 1999; Krylyshkina et al., 2003). This form of MT–actin cross talk was first reported almost 20 years ago, and yet our understanding of the underlying mechanisms remains limited. It is still unclear how MT plus ends are stabilized or captured by FAs, although this may involve the formin Dia1 (Ballestrem et al., 2004) and interactions between KANK and Talin (Bouchet et al., 2016). In addition, it is only partially understood how the arrival of MT plus ends triggers FA disassembly. Previous studies suggest that this process involves clathrin- and dynamin-mediated endocytosis of FA components (Ezratty et al., 2005, 2009), MT delivery of exocytic vesicles carrying MMP to degrade integrin–ECM links (Stehbens et al., 2014), and NBR1-dependent autophagy (Kenific et al., 2016). Our findings reveal an additional requirement for APC-mediated actin assembly: given its dual affinity for MTs and actin, APC could play a role in stabilizing or capturing MT ends at FAs, possibly together with formins. Indeed, APC and Dia formins have both been shown to be critical for capturing MT ends at the leading edge of migrating cells (Zaoui et al., 2008, 2010; Daou et al., 2014). Alternatively, APC (alone or with formins) may stimulate actin assembly at FAs to help drive endocytosis, autophagy, and/or exocytic vesicle delivery.

Finally, we note that our APC (m4) mutant effects were dominant in vivo, similar to the cancer-linked C-terminal truncations of APC, which dimerize with intact FL-APC (Kinzler et al., 1991). FL-APC (m4) mutant may therefore exert dominant effects in a related manner. This in turn raises the possibility that loss of APC's MT and/or actin regulatory functions caused by C-terminal truncations contributes to the altered migration of colonic crypt epithelial cells in colorectal tumorigenesis. With the mutant tool we have generated in this study, it will now be possible to rigorously test this model in animals.

Materials and methods

Plasmid construction

To generate plasmids for *Escherichia coli* expression of APC-B truncations (C2560 or C2542), appropriate sequences were PCR amplified from pBG721, a plasmid for expression of the WT APC Basic domain (2,167–2,674; Moseley et al., 2007), and subcloned into EcoRI–NotI sites of the same vector. The following oligos were used: forward, 5′-GCCACTGAATTCTAAAACCAGGGGAGAAAAGTACATTGG-3′, and reverse, 5′-AAAAAAGCGGCCGCTCAGTGATGGTGATGGTGATGACTGGATTCTGATGAAGCAGAAAGAAT-3′; or forward, 5′-GCCACTGAATTCTAAAACCAGGGGAGAAAAGTACATTGG-3′, and reverse, 5′-ATCGCTGCGGCCGCTCAGTGATGGTGATGGTGATGATTGATTGGAAGTCTAGAAGGACTTTC-3′.

Site-directed mutagenesis was used to generate the four APC-B mutants (m1–m4). The oligos used were as follows. For m1 (D2527A I2528A), we used forward, 5′-CCAGCAAAGCGCGCTGCTGCACGGTCTCATTCTGAAAGT-3′, and reverse, 5′-ACTTTCAGAATGAGACCGTGCAGCAGCATGGCGCTTTGCTGG-3′. For m2 (H2532A E2534A), we used forward, 5′-CATGATATTGCACGGTCTGCTTCTGCAAGTCCTTCTAGACTT-3′, and reverse, 5′-AAGTCTAGAAGGACTTGCAGAAGCAGACCGTGCAATATCATG-3′. For m3 (D2527A I2528A R2530A S2531A), we used forward, 5′-CCAGCAAAGCGCGCTGCTGCAGCGGCTCATTCTGAAAGT-3′, and reverse, 5′-ACTTTCAGAATGAGCCGCTGCAGCAGCAGCGCGCTTTGCTGG-3′. For m4 (L2539A P2541A), we used forward, 5′-GAAAGTCCTTCTAGAGCTCCAGCCAATAGGTCAGGAACC-3′, and reverse, 5′-GGTTCCTGACCTATTGGCTGGAGCTCTAGAAGGACTTTC-3′. Underlined nucleotides indicate the ones changed from the WT sequence to produce the mutations. The m4 oligos were also used for site-directed mutagenesis to generate SNAP-649–APC-C (m4) (L2539A P2541A), starting from the pBG993 SNAP-649–APC-C plasmid (Breitsprecher et al., 2012).

To generate plasmids for expression and purification of the CC-APC-B (WT and m4) chimeric polypeptides, primers encoding the N-terminal CC domain of APC (1–55) flanked by BamHI and EcoRI sites (forward, 5′-GATCCATGGCTGCAGCTTCATATGATCAGTTGTTAAAGCAAGTTGAGGCACTGAAGATGGAGAACTCAATCTTCGACAAGAGCTAGAAGATAATTCCAATCATCTTACAAAACTGGAAACTGAGGCATCTAATATGAAGGAAGTACTTAAACAACTACAAGG-3′, and reverse, 5′-AATTCCTTGTAGTTGTTTAAGTACTTCCTTCATATTAGATGCCTCAGTTTCCAGTTTTGTAAGATGATTGGAATTATCTTCTAGCTCTTGTCGAAGATTTGAGTTCTCCATCTTCAGTGCCTCAACTTGCTTTAACAACTGATCATATGAAGCTGCAGCCATG-3′) were annealed and then subcloned into pGEX-6p–harboring APC-B (WT or m4).

An RNAi-refractive WT FL human APC rescue plasmid (for expression of untagged FL-APC protein in cultured cells) was generated by introducing silent mutations at specific nucleotides (370, 373, 376, and 379) by site-directed mutagenesis using oligos 5′-CGGGAAGGATCAGTGTCCAGACGTTCTGGAGAGTGC-3′ (sense) and 5′-GCACTCTCCAGAACGTCTGGACACTGATCCTTCCCG-3′ (antisense) on the pCMV-Neo-Bam–APC plasmid (16507; Addgene). The same oligos were used to introduce the same RNAi-refractive mutations into pGFP–FL-APC (WT) (a gift from A. Barth, Stanford University, Palo Alto, CA) for expressing GFP–FL-APC proteins in cells. Next, the m4 point mutations were introduced by site-directed mutagenesis into RNAi-refractive pCMV-Neo-Bam–APC. To generate the mutant

tailed Student's *t* test. (D) Representative images of cells as in A stained with phospho-Paxillin antibodies. Magnifications correspond to boxed regions. (E) Quantification of FA size (surface area) measured by phospho-Paxillin immunostaining as in D. Data averaged from three independent experiments (n = 30 FAs per condition). (F) Quantification of FA density at the cell periphery in boxed (10 × 10 µm) regions. Data averaged from three independent experiments (n = 20 boxes per condition). (E and F) Error bars, SEM; one-way ANOVA Holm-Sidak's multiple comparison test. (G) Representative images of cells treated as in D stained with antibodies against phospho-Paxillin (gray) or tubulin (magenta). Merge panels show overlap of signals, and magnification is from boxed regions. (H) Time-lapse TIRF imaging of FAs marked by GFP-Paxillin in cells treated as in A. Images show overlay of GFP-Paxillin signal at 0 min and 20 min, with two representative magnifications from boxed regions per condition. (I) Thresholded-Mander's correlation coefficient (*t*M1 and *t*M2) value of GFP-Paxillin signal overlap at 0 and 20 min from 10 cells as in H. Significant differences: *, $P < 0.05$; **, $P < 0.01$; ***, $P < 0.001$; ****, $P < 0.0001$; n.s., not significant.

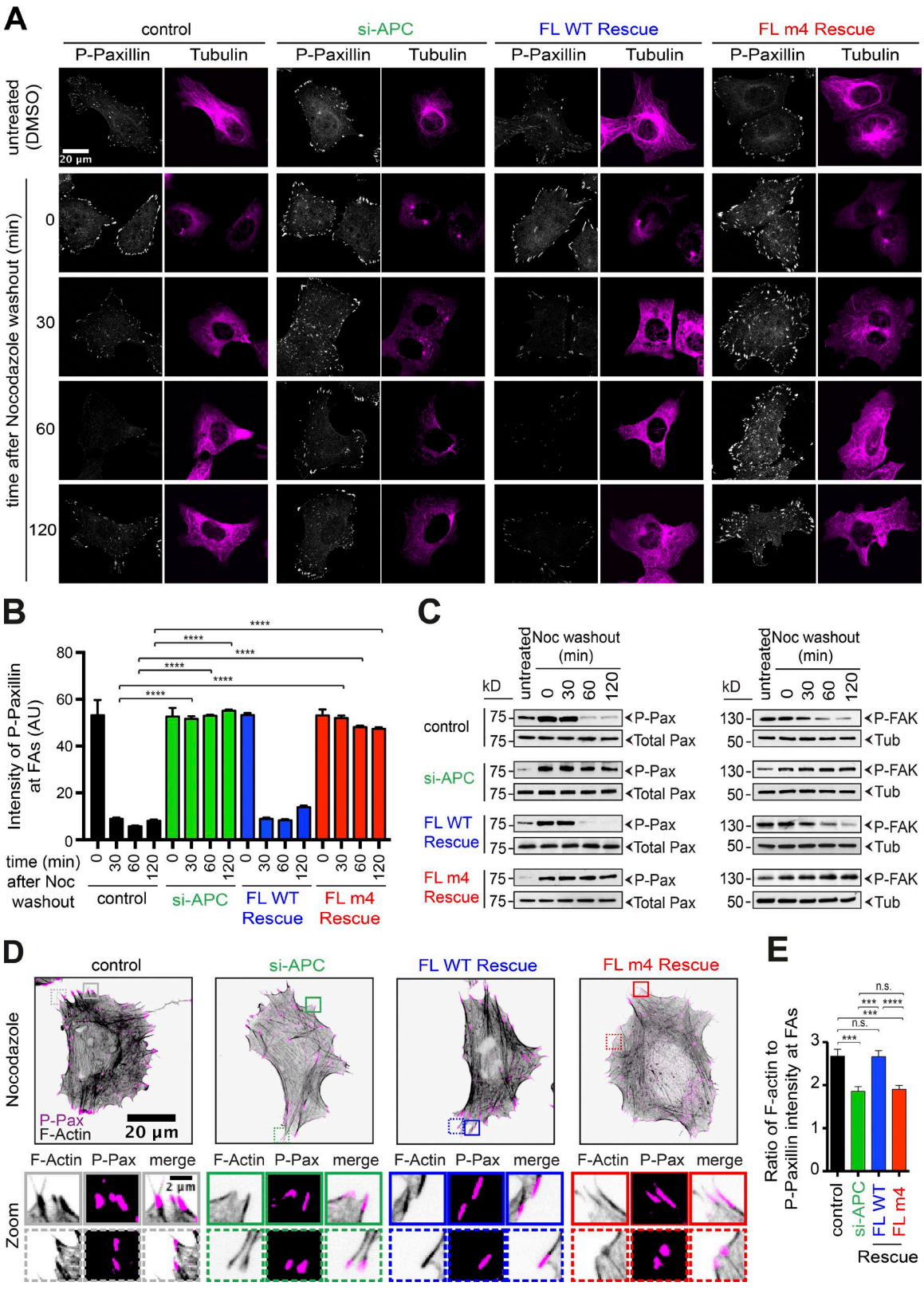

Figure 5. **Expression of mutant (m4) FL-APC leads to reduced F-actin levels at FAs and severe defects in MT-induced FA turnover.** (A) Representative images of FA turnover cells after nocodazole treatment and washout at different time points. Cells from mock-treated (control) U2OS cells, cells depleted of endogenous APC (si-APC), and depleted cells rescued by plasmids expressing si-resistant FL-APC constructs (rescue FL-WT and FL-m4) were treated with nocodazole, and then the drug was washed out with serum-free media and cells were immunostained with phospho-Paxillin and tubulin antibodies. (B) Quantification of integrated fluorescence intensity of individual FAs measured from phospho-Paxillin immunostaining images as in A. Data were normalized to control cells treated with nocodazole before washout and averaged from three independent experiments ($n \geq 1{,}500$ FAs per condition from 20 cells). Error bars, SEM; one-way ANOVA Holm-Sidak's multiple comparison test. (C) Western blot analysis of phospho-Paxillin (P-Pax), total Paxillin, FAK-pY397

GFP–FL-APC (m4) plasmid, we subcloned a SwaI–BamHI fragment (spanning the region mutated by m4) from pCMV-Neo-Bam–APC into the corresponding sites in pGFP–FL-APC (WT).

Protein purification

Rabbit skeletal muscle actin (RMA) was purified as described previously (Spudich and Watt, 1971). In brief, RMA was purified first by generating an acetone powder from ground muscle tissue, which was stored in aliquots at −80°C. Then, aliquots of acetone powder were pulverized using a coffee grinder, resuspended in G buffer (5 mM Tris-HCl, pH 8.0, 0.2 mM ATP, 0.2 mM $CaCl_2$, and 0.2 mM DTT), and cleared by low-speed centrifugation. The actin was polymerized overnight and then pelleted. The pellet was disrupted by douncing, dialyzed against G buffer for 2–3 d, and then aliquoted and stored at −80°C until use. Every 2 wk, fresh RMA was prepared by thawing an aliquot of actin, dialyzing against G buffer for 1–2 d, clearing by ultracentrifugation, and gel filtering the supernatant on a 16/60 S200 column (GE Healthcare). Column fractions were stored at 4°C.

For use in bulk actin assembly assays, RMA was fluorescently labeled with *N*-(1-pyrenyl) iodoacetamide on cysteine 374 (Cooper et al., 1984). RMA prepared excluding the gel-filtration step was dialyzed against pyrene buffer (25 mM Tris-HCl, pH 7.5, 100 mM KCl, 0.02% NaN_3, 0.3 mM ATP, and 2 mM $MgSO_4$) for 3–4 h and then diluted with pyrene buffer to 1 mg/ml (23.8 µM). A sevenfold molar excess of pyrenyl-iodoacetamide was added, the actin solution was incubated overnight at 4°C, and then aggregates were cleared by low-speed centrifugation. The supernatant (containing F-actin) was centrifuged for 3 h at 4°C at 45,000 rpm in a rotor (Ti70; Beckman Coulter) to pellet F-actin. The actin pellets were disrupted by douncing, dialyzed against G buffer for 1–2 d, and gel filtered on a 16/60 S200 column as above. Peak fractions were pooled, aliquoted, snap frozen, and stored at −80°C until use.

For TIRF microscopy assays, the concentration and degree of RMA labeled with Oregon green (OG-labeled actin) were determined as described previously (Kuhn and Pollard, 2005). The labeling procedure was the same as above for pyrene labeling, except that a 10-fold molar excess of OG 488 iodoacetamide (Molecular Probes) was used instead of the sevenfold molar excess of pyrenyl-iodoacetamide.

C-Daam1 (FH1-FH2-C) and C-mDia1 (FH1-FH2-C) were expressed in *Saccharomyces cerevisiae* strain BJ2168 from 2-µm plasmids as 6His-fusion proteins under galactose-inducible promoters (Moseley et al., 2004). In brief, for each formin polypeptide, 2 liters of yeast cells were grown in synthetic medium lacking uracil and 2% raffinose to OD_{600} = 0.8, and then expression was induced by addition of galactose (2% final), and cells were grown for another 8–12 h at 30°C. Cells were then washed in H_2O, frozen under liquid N_2, and lysed by mechanical disruption using a coffee grinder and liquid N_2. The resulting frozen yeast powder was stored at −80°C until use. C-Daam1 and C-mDia1 were then purified as described previously (Moseley et al., 2004; Jaiswal et al., 2013a). In brief, 10 g of frozen yeast powder was resuspended in buffer A (30 mM imidazole, pH 8.0, 0.5 mM DTT, and 2× PBS [40 mM sodium phosphate buffer and 200 mM NaCl, pH 7.4]) also containing 150 mM NaCl, 1% NP-40, standard protease inhibitors, and 2 mM PMSF, until all clumps were dissolved, and then cleared by ultracentrifugation at 300,000 *g* for 20 min at 4°C in a rotor (TLA100.3; Beckman Coulter). The supernatant was incubated with 500 µl nickel–nitrilotriacetic acid (Ni-NTA)–agarose beads (Qiagen) for 2 h at 4°C, and then the beads were washed three times with buffer A containing 350 mM NaCl, followed by three additional washes with buffer A. Proteins were eluted with buffer A supplemented with 350 mM imidazole, pH 8.0, and 0.5 mM DTT. Eluted proteins were purified further on a gel filtration column (Sup6; GE Healthcare) equilibrated in buffer $HEKG_5D$ (20 mM Hepes, pH 7.5, 1 mM EDTA, 50 mM KCl, 5% [vol/vol] glycerol, and 1 mM DTT) using fast protein liquid chromatography (AKTA; GE Healthcare). Peak fractions were pooled, concentrated in Amicon Ultra centrifugal concentrators (Millipore), aliquoted, snap frozen, and stored at −80°C.

Human profilin was purified as described previously (Kovar et al., 2006). In brief, a plasmid expressing human profilin (Kovar et al., 2006) was transformed into BL21(DE3) *E. coli* cells, which were then grown to OD_{600} = 0.5 in Terrific Broth plus antibiotics. Protein expression was induced for 3 h at 37°C with 0.4 mM IPTG. Cells were harvested by centrifugation, flash frozen, and stored at −80°C. Cell pellets were resuspended in lysis buffer (50 mM Tris, pH 8.0, DNase, lysozyme, and complete protease inhibitors), kept in ice for 20 min, and then lysed by sonication (four pulses of 30 s). Lysates were cleared for 30 min at 14,000 rpm, and then the supernatant was collected, diluted to 5 ml, loaded on a Q_{FF} column (GE Healthcare) equilibrated in 20 mM Tris, pH 8.0, and 50 mM NaCl, and eluted with a salt gradient (0–1 M NaCl and 20 mM Tris, pH 8.0). Peak fractions were pooled, concentrated, and further purified on a column (Superdex 75; GE Healthcare) equilibrated with 20 mM Tris, pH 8.0, and 50 mM NaCl. Peak fractions were pooled, concentrated, aliquoted, snap frozen, and stored at −80°C.

Human CapZ was purified as described previously (Amatruda and Cooper, 1992). In brief, a plasmid expressing human CapZ (Soeno et al., 1998) was transformed into BL21(DE3) pLysS *E. coli* cells, and cells were grown to OD_{600} = 0.8 in Luria-Bertani broth plus antibiotics. Protein expression was induced for 3 h at 37°C with 0.4 mM IPTG. Cells were harvested by centrifugation, flash frozen, and stored at −80°C. Cell pellets were resuspended in lysis buffer (20 mM Tris-Cl, pH 8.0, 1 mM EDTA, 0.2% Triton X-100, lysozyme, and complete protease inhibitors), kept on ice for 30 min, and then lysed by sonication (four pulses of 30 s). Lysates were cleared for 30 min at 14,000 rpm at 4°C, and the supernatant was collected and loaded on a column (Q_{FF}; GE Healthcare) equilibrated in 20 mM Tris, pH 8.0, and 50 mM NaCl and eluted with a salt gradient (0–1 M NaCl and 20 mM Tris, pH 8.0). Peak fractions were pooled, concentrated, and further fractionated on a column (Superdex 75) equilibrated with 20 mM Tris, pH 8.0, and 50 mM NaCl. Peak fractions were pooled and further purified on a monoQ column and eluted with a salt gradient (20 mM Hepes, pH 6.8, 1 mM EDTA, and 0–500 mM KCl). Peak fractions were pooled and dialyzed overnight into HEK buffer (20 mM Hepes, pH 7.5, 1 mM EDTA, and 50 mM KCl), snap frozen in aliquots, and stored at −80°C.

All APC-B (WT, mutant, and truncated), CC-APC-B, and SNAP–APC-C polypeptides were purified essentially as described previously (Okada et al., 2010; Breitsprecher et al., 2012) with the following minor modifications. In brief, plasmids expressing APC constructs were transformed into *E. coli* BL21(DE3) pLysS cells, and cells

(P-FAK), and tubulin (Tub; loading control) levels in U2OS cells grown on plastic dishes, which is distinct from the cells in A grown on collagen-coated glass coverslips. This difference results in small differences in the timing of FA disassembly in A versus C. (D) Representative images of cells treated with nocodazole for 3 h showing merge of F-actin organization (rhodamine-phalloidin) and FAs (P-Paxillin). For each condition, representative magnifications of two boxed regions are shown. (E) Quantification of the ratio of fluorescence intensity of the F-actin signal to the phospho-Paxillin signal at individual FAs, measured from images as in D. Data were averaged from three independent experiments (>700 individual FAs and *n* = 50 cells per condition). Error bars, SEM; one-way ANOVA Holm-Sidak's multiple comparison test. Statistical differences: ***, P < 0.001; ****, P < 0.0001; n.s., not significant.

were grown to OD_{600} = 0.8 in Terrific Broth plus antibiotics. Protein expression was induced for 4 h at 37°C with 0.4 mM IPTG. Cells were harvested by centrifugation, flash frozen, and stored at −80°C. Cell pellets were resuspended in cold lysis buffer (30 mM Tris, pH 8.0, 600 mM KCl, 1 mM EDTA, pH 8.0, 1 mM DTT, DNase, lysozyme, complete protease inhibitor cocktail, and 0.2 mM PMSF), homogenized by douncing, and then lysed by sonication (four pulses of 30 s). Lysates were cleared for 30 min at 33,500 *g*, and the supernatant was mixed with 0.5 ml glutathione-agarose beads (Thermo Fisher Scientific) and incubated for 1 h at 4°C. Then, beads were washed three times in 30 mM Tris, pH 8.0, 600 mM KCl, and 1 mM EDTA, pH 8.0, and proteins were eluted in the same buffer plus 5% glycerol and 30 mM glutathione. Eluted proteins were mixed with 0.5 ml Ni-NTA–agarose beads in 30 mM Tris, pH 8.0, 600 mM KCl, and 1 mM EDTA, pH 8.0, and 1% Triton X-100 plus 30 mM imidazole and incubated for 1 h at 4°C. Beads were then washed three times in the same buffer lacking detergent, and fractions were eluted in the same buffer plus 300 mM imidazole. Peak fractions were pooled, dialyzed into $HEKG_5$ buffer (20 mM Hepes, pH 7.5, 1 mM EDTA, 50 mM KCl, and 5% glycerol), aliquoted, snap frozen, and stored at −80°C. SNAP-tagged APC proteins were purified in the same manner, except while still on the Ni-NTA–agarose beads, they were fluorescently labeled overnight at 4°C using 50 µM dye (SNAP-surface649; New England Biolabs). Beads were then washed five times to remove excess dye, and proteins were eluted, dialyzed, aliquoted, and stored. Percent labeling of SNAP–APC-C (WT and m4) was determined by measuring fluorophore absorbance in solution using the extinction coefficient SNAP–surface 649:ε655 = 250,000 M^{-1} cm^{-1}. SNAP–APC-C (WT and m4) labeling efficiencies were 88% and 77%, respectively. Concentrations of all proteins were determined by band intensity on Coomassie-stained gels compared with a BSA standard curve using an Odyssey imaging system (LI-COR Biotechnology).

Bovine brain tubulin was purified essentially as described previously (Goode et al., 1999; Castoldi and Popov, 2003). In brief, tubulin was isolated from freshly prepared bovine brain lysates by three rounds of temperature-controlled polymerization and depolymerization. The final MT pellet was mechanically disrupted by douncing and depolymerizing on ice and then further purified on a phosphocellulose column equilibrated in PME buffer (80 mM KOH-Pipes, pH 6.8, 1 mM $MgCl_2$, 1 mM EGTA, and 1 mM GTP). Tubulin was found in the flow-through and then was loaded directly onto a DEAE column and eluted with a linear salt gradient (0.1–0.6 M NaCl) in PME buffer. Peak fractions were pooled, desalted, concentrated to 80 µM, aliquoted, snap frozen, and stored at −80°C.

Bulk fluorescence actin assembly assays

Monomeric actin (2 µM; 5% pyrene labeled) in G buffer was converted to Mg-ATP-actin immediately before each reaction as described previously (Moseley and Goode, 2005). Actin was mixed with proteins or control buffer, and then 3 µl of 20× initiation mix (40 mM $MgCl_2$, 10 mM ATP, and 1 M KCl) was added to initiate polymerization. Fluorescence was monitored at an excitation of 365 nm and emission of 407 nm at 25°C in a fluorimeter (Photon Technology International). Actin assembly rates were determined from the slopes of the polymerization curves during the first 200 s. For all assembly assays, at least three independent experiments were performed using different stocks of purified APC-B (WT, truncated, and point mutants).

In vitro TIRF microscopy and data analysis

Glass coverslips (60 × 24 mm; Thermo Fisher Scientific) were cleaned and prepared as described previously (Breitsprecher et al., 2012). In brief, flow cells were assembled by adhering sonicated poly-ethylene glycol–silane-coated coverslips preincubated at 70°C overnight to µ-Slide VI0.1 (0.1 × 17 × 1 mm) flow chambers (Ibidi) with double-sided tape (2.5 cm × 2 mm × 120 µm) and 5-min epoxy resin (Devcon). Before each reaction, 4 µg/ml streptavidin in HEK buffer (20 mM Hepes, pH 7.4, 1 mM EDTA, and 50 mM KCl) was flowed in for 15 s, followed by washing with HEK buffer and 1% BSA. The flow cell was then equilibrated with TIRF buffer (10 mM Hepes, pH 7.4, 50 mM KCl, 1 mM $MgCl_2$, 1 mM EGTA, 0.2 mM ATP, 10 mM DTT, 15 mM glucose, 20 µg/ml catalase, 100 µg/ml glucose oxidase, 10 mM imidazole, and 0.5% methylcellulose [4,000 cP]). Where indicated, APC-B and other proteins were diluted into TIRF buffer and then rapidly mixed with 1 µM actin monomers (10% OG labeled and 0.2% biotinylated) and introduced into the flow cell using a syringe pump (Harvard Apparatus). The flow cell was then immediately mounted on the microscope stage for imaging. The delay between mixing of proteins and initial imaging was 30 s. Time-lapse TIRF imaging was performed using an inverted microscope (Ti200; Nikon Instruments) equipped with 100-mW solid-state lasers (Agilent Technologies), a chrome-free infinity Apo 60× 1.49 NA oil-immersion TIRF objective (Nikon Instruments), an electron-multiplying charge-coupled device camera with a pixel size of 0.267 µm (Andor Ixon), and an additional 1.5× zoom module (Nikon Instruments). Focus was maintained using the Perfect Focus System (Nikon Instruments), and frames were captured every 5 s for a total of 600 s (10 ms at 488 nm of excitation and 10% laser power) using Imaging Software Elements (Nikon Instruments). Image analysis was performed in ImageJ (National Institutes of Health). Background fluorescence was removed from each time series using the background subtraction tool (rolling ball radius of 50 pixels) in Fiji. For measuring the number of actin filaments nucleated in TIRF reactions, each field of view (FOV) was examined 300 s after initiation of actin assembly. For single-molecule colocalization experiments, 1 µM OG-actin monomers were incubated for 30 min with 10 µM Latrunculin B, mixed and incubated with 20 nM SNAP-649–APC-C (WT or m4) for 30 min, and then diluted 20-fold in TIRF buffer and introduced into a TIRF flow chamber for imaging. For step photobleaching analysis, 0.5 nM SNAP-649–APC-C (WT and m4) in TIRF buffer without glucose oxidase or catalase was passively absorbed to the coverslip and then exposed to constant illumination at high laser power (80% at 100 mW) and imaged every 0.1 s by TIRF. Background fluorescence was subtracted using the background subtraction tool (rolling ball radius of 20 pixels) implemented in ImageJ. The oligomeric states of SNAP-649–APC-C molecules (WT and m4) were determined by comparing distributions of the number of photobleaching events to probability distributions for the number of fluorescent subunits calculated from the binomial distribution as described previously (Breitsprecher et al., 2012).

In vitro F-actin binding and bundling assays

For most of the binding and bundling assays (Fig. S2, A and B), 20 µM-monomeric actin was polymerized for 1 h at 25°C in F buffer (G buffer plus 1× initiation mix) and then diluted in F buffer to different concentrations (2, 4, and 8 µM). F-actin was incubated for 10 min with or without 0.5 µM precleared APC-B (WT or m4) polypeptides and centrifuged for 30 min at 350,000 *g* (high-speed pelleting, F-actin binding assays) or 5 min at 8,600 *g* (low-speed pelleting, F-actin bundling assays). For the remaining F-actin bundling assays (Fig. S2 C), variable concentrations of WT or m4 APC-B (0.05, 0.1, 0.2, and 0.5 µM) were incubated with a fixed concentration (3 µM) of F-actin. Supernatants and pellets were analyzed on Coomassie-stained gels.

In vitro MT binding and bundling assays

For MT cosedimentation and MT bundling assays (Fig. S2, D and E), 20 µM bovine brain tubulin was polymerized for 30 min at 35°C in

MT buffer (25 mM Pipes, pH 6.8, 3 mM $MgCl_2$, 1 mM EGTA, and 1 mM GTP) and then stabilized by the addition of 20 µM Taxol. MTs were diluted fivefold in MT buffer and 2 µM Taxol, mixed with 0.6 µM precleared APC-B (WT or m4), incubated for 10 min at room temperature, and centrifuged for 30 min at 157,000 *g* (MT binding assays) or 3 min at 8,600 *g* (MT bundling assays). Supernatants and pellets were analyzed on Coomassie-stained gels.

Protein interaction assays

For testing APC–Daam1 interactions (Fig. S2 H), GST–APC-B was immobilized on glutathione-agarose beads in binding buffer (20 mM Hepes, pH 7.4, 50 mM KCl, and 1 mM DTT). Beads were washed and then mixed (final concentration of 0.5 µM GST–APC-B) with 0.25 µM 6× His-tagged C-Daam1 and incubated for 1 h at 4°C. Beads were pelleted and washed, and supernatants and pellets were analyzed on Coomassie-stained gels. For measuring G-actin binding, 100 nM Ca-ATP–G-actin (100% pyrene labeled) was incubated for 5 min with 100 nM Latrunculin B in G buffer. Then, 55 µl of this mixture was mixed with 5 µl APC-B (WT or m4) at different concentrations (0–100 nM) in $HEKG_5$ buffer and incubated for at least 2 min at room temperature to reach steady state, and then pyrene fluorescence was measured in a fluorimeter at 25°C using an excitation of 365 nm and an emission of 407 nm.

Cell culture, transfection, and RNAi silencing

Human osteosarcoma (U2OS) and human breast cancer (MDA-MB-231) cell lines (ATCC or ATCC-LGC standards, respectively) were grown in DMEM (Gibco BRL Life Technologies) supplemented with 200 mM L-glutamine (Thermo Fisher Scientific) and 10% FBS at 37°C and 5% CO_2. U2OS cells were transfected using Lipofectamine 3000 (Thermo Fisher Scientific) according to the manufacturer's instructions in plastic 6-well plates. MDA-MB-231 cells were transfected with siRNA oligos using Lipofectamine RNAiMAX or plasmids using Lipofectamine 2000 (Thermo Fisher Scientific). To silence APC, 60,000 U2OS cells were transfected with 30 pmol RNAi oligos, or 150,000 MDA-MB-231 cells were reverse transfected with 0.15 pmol RNAi oligos directed against the human APC mRNA coding region: sense, 5′-GGAUCUGUAUCA AGCCGUUTT-3′, and antisense, 5′-AACGGCUUGAUACAGAUC CTT-3′. Cells were transfected in parallel with control "scramble" RNAi oligos 5′-CAGUCGCGUUUGCGACUGG-3′ with dTdT 3′ overhangs. Transfection and silencing efficiencies were optimized for consistency and high efficiency (80–90%) by tittering the loads of oligos and plasmids. Western blotting and immunofluorescence validated that endogenous APC was silenced 48 h after transfection. For silence and rescue experiments, cells were first transfected with oligos, transfected with rescue plasmids 24 h later, and fixed for immunofluorescence or alternatively used for live imaging another 24 h later. For U2OS cells and MDA-MB-231 cells, we used 1 and 2 µg APC rescue plasmid, respectively. Rescue plasmids express RNAi-resistant FL-APC (WT or m4). For ectopic expression, the same amounts of plasmids were transfected, but without prior transfection with oligos. To examine APC localization at FAs (Fig. 4 A), U2OS cells were cotransfected with 600 ng of a mCherry-Zyxin plasmid (55166; Addgene) and 600 ng of a plasmid expressing GFP-tagged FL-APC (WT or m4). Cells were imaged 12 h after transfection by TIRF microscopy on the inverted microscope (Ti200) described above but exposing for 15 ms at 488-nm excitation and for 5 ms at 633-nm excitation, both at 10% laser power, and maintaining cells at 37°C using a heated stage (Ibidi). Images were acquired using Nikon Elements software, and image analysis was performed in ImageJ.

Western blotting

To measure APC levels in cells after silencing and rescue, cells were collected 48 h after initial oligo transfection and incubated for 30 min at 4°C in lysis buffer (150 mM NaCl, 1.0% NP-40, 0.5% sodium deoxycholate, 0.1% SDS, 50 mM Tris, pH 7.5, 2 mM EDTA, 0.2 mM sodium orthovanadate, 20 mM β-glycerolphosphate, 50 mM sodium fluoride, 1 mM PMSF, 1 mM DTT, and 1× Roche complete protease inhibitor mixture). Samples were precleared by centrifugation at 14,000 rpm for 30 min at 4°C, quantified by Bradford assay, and immunoblotted. For measuring phospho-Paxillin, total Paxillin, and phospho–FAK-pY397 levels, the same procedure was used except that cells were incubated in serum-free media overnight before collection. Blots were probed with 1:500 rabbit anti-APC (ab15270; Abcam), 1:2,000 rabbit anti–GFP (ab6556; Abcam), 1:500 rabbit anti–phospho-Paxillin (Tyr118; PP4501; ECM Biosciences), 1:1,000 rabbit anti–FAK-phospho–tyrosine 397 (FAK-pY397; 141–9; Invitrogen), 1:1,000 mouse/human anti-Paxillin (AHO0492; Invitrogen), or 1:2,000 mouse anti–α-tubulin antibody (sc-32292; Santa Cruz Biotechnology). Blots were then probed with secondary horseradish peroxidase antibodies (GE Healthcare), and proteins were detected using a Pierce ECL Western Blotting Substrate detection kit (Thermo Fisher Scientific). Bands were quantified using Fiji.

Immunostaining cells

For cell-staining experiments, 48 h after transfection, the cells were replated for 2–5 h on 3 × 1 × 1–mm glass coverslips (VWR International) that had been acid washed and coated with collagen I (Advanced BioMatrix). Cells were then fixed for 15 min with 4% paraformaldehyde in 1× PBS (2.7 mM KCl, 1.8 mM KH_2PO_4, 10 mM Na_2HPO_4, and 140 mM NaCl, pH 7.4) at room temperature and then permeabilized for 15 min in 1× PBS plus 0.5% Triton X-100 and 0.3 M glycine. Cells were blocked for 1 h at room temperature in 3% BSA dissolved in PBST (1× PBS and 0.1% Tween 20) and incubated for 12 h with 1:300 rabbit anti-APC antibody (ab15270; Abcam), 1:1,000 mouse anti–α-tubulin antibody (sc-32292; Santa Cruz Biotechnology), 1:1,000 rabbit anti–phospho-Paxillin (Tyr118; PP4501; ECM Biosciences), or 1:1,000 mouse antivinculin (V9131; Sigma). Coverslips were washed three times with 1× PBST and incubated for 1 h at room temperature with different combinations of secondary antibodies (Thermo Fisher Scientific): 1:1,000 donkey anti–rabbit Alexa Fluor 488 (A-21206), 1:2,000 donkey anti–mouse Alexa Fluor 649 (A-31571), 1:1,000 goat anti–mouse Alexa Fluor 633 (A-21050), and 1:2,000 goat anti–rabbit Alexa Fluor 633 (A-21071). F-actin was stained with 1:1,500 rhodamine-phalloidin (R415; Life Technologies). After three washes with PBS plus 0.1% Tween 20 and one wash with PBS, coverslips were mounted with AquaMount (Thermo Fisher Scientific). Cells were imaged on a laser-scanning confocal inverted eclipse microscope (Ti-E-PFS3; Nikon Instruments) equipped with a 100-mW solid-state laser and emission tuner for 488-, 561-, and 640-nm wavelengths, a 60× (NA 1.40) oil-immersion objective, a C2 imaging head (Nikon Instruments), and a 7-LED Light Engine array and sCMOS camera (Andor Zyla) at room temperature. Images were acquired using Nikon Elements software (version 4.30.02) with 2× averaging stacks (nine plane stacks and 0.5-µm steps) at 1–2% laser power during 60–80 ms of exposure. Maximum intensity projections and raw fluorescence values were measured using Fiji.

To quantify overall F-actin density in cells (Fig. 2 C), transfected cells were grown on collagen-coated glass coverslips, fixed in 4% paraformaldehyde in PBS for 15 min, processed for immunofluorescence as above, and stained with rhodamine-phalloidin. Cells were imaged using an inverted eclipse microscope (Ti-E-PFS3) as above. Maximum intensity projections were generated, and then individual cells were cropped and the raw fluorescence intensities of the cells (n = 60 per condition) were quantified in Fiji and divided by cell area to calculate density. To quantify F-actin density at FAs (Fig. 5 E), transfected cells

were grown as above, treated with 10 µM nocodazole in serum-free medium for 3 h, fixed as above, stained with rhodamine-phalloidin and with 1:1,000 rabbit anti–phospho-Paxillin (Tyr118; PP4501; ECM Biosciences), and then stained with 1:1,000 donkey anti–rabbit Alexa Fluor 488 (A-21206; Invitrogen). Cells were imaged on an inverted eclipse microscope (Ti-E-PFS3) as above. Maximum intensity projections were generated, individual cells (n = 50 per condition) were cropped, and the ratio of integrated fluorescence intensity of F-actin versus phospho-Paxillin at each individual FA (>700 per condition) was quantified in an automated fashion using a custom script in ImageJ. To quantify MT density at the leading edge, a box (20 × 20 µm^2) was positioned at the cell edge, extending back toward the center of the cell, and mean fluorescence intensity was measured in the box using Fiji. To examine mitochondrial distribution, transfected cells were stained with 20 nM MitoTracker green FM probe (Thermo Fisher Scientific) for 5 min at 37°C and then washed four times with prewarmed PBS. Cells were then imaged on an inverted eclipse microscope (Ti-E-PFS3) as above, and then Fiji was used to generate maximal intensity projections and quantify mitochondrial distribution in cells.

Wound-healing assays

U2OS cells (10^6) were plated on collagen-coated glass-bottom dishes (MatTek Corporation), and then cells were transfected with siRNA oligos and/or plasmids as above. Confluent cells were stained for 5 h with SiR-actin F-actin labeling probe (SC001; Cytoskeleton Inc). Then, wounds were created by scraping the monolayer with a pipette tip. The dishes were washed with 1× PBS and replenished with DMEM containing high-glucose buffer (Gibco BRL Life Technologies) supplemented with 10 mM sodium bicarbonate, pH 7.4, 10% FBS, 20 mM L-glutamine, and 1 mM sodium pyruvate. Wound closure was monitored at 10-min intervals for a duration of 20 h, maintaining cells at 37°C with 5% CO_2 using a controller (Okolab) adapted to the inverted eclipse microscope (Ti-E-PFS3). Images were captured using a 10× (NA 0.3) air objective. Although there was some variation in wound size from dish to dish, a large number of wounds were analyzed, and the mean wound size was not significantly different between conditions (Fig. 2 C). Wound-healing assays were also performed using transfected cells but with the addition of a GFP-actin plasmid (a gift from D. Kast and R. Dominguez, University of Pennsylvania, Philadelphia, PA). Assays were performed as above, except that the cells were replated on dishes containing a sterile silicone insert (Ibidi) that patterns cells around an open gap. After cells grew to confluency, the silicone insert was removed, creating a gap (wound) for cells to migrate into, and cells were imaged. Movements of individual cells were tracked using ImageJ. For each cell, its positional coordinates relative to the nucleus were recorded every five frames (50 min) until the scratch wound was closed. Custom scripts in MATLAB (MathWorks) were used to analyze cell migration paths to determine total distance of migration (L) and net distance traveled between starting and end points (D). From these measurements, we calculated for each cell its L/D ratio and its mean speed of movement.

Chemotaxis assays

MDA-MB-231 cells were grown on collagen-coated glass coverslips in Dunn chemotaxis chambers (Hawksley Technology) and then transfected with siRNA oligos and/or plasmids as above. Next, a stable chemotactic gradient of FBS was generated by placing DMEM containing 10% FCS in the outside well and DMEM in the inside well. Cell migration paths were recorded using a microscope (Axiovert 200; Zeiss) equipped with a digital camera (CoolSnap HQ; Roper Scientific) running MetaMorph 6.3 software and a 10× plan Apochromat (NA 1.4) objective, acquiring images every 8 min for 64 min, keeping cells at 37°C. For each condition, at least 150 individual cells were tracked, and data were analyzed in ImageJ using the Chemotaxis and Migration Tool to determine Y forward index migration (Foxman et al., 1999). Statistical analysis was performed with Prism 6.0 (GraphPad).

Live-cell imaging of MT plus end dynamics

U2OS cells were transfected in 6-well plates except with 200 ng of plasmid expressing GFP-EB1 (Henty-Ridilla et al., 2016). 48 h after transfection, cells were replated on glass-bottom dishes and grown for another 5 h. Then, the media was replaced with RPM1 buffer (Thermo Fisher Scientific) supplemented with 20 mM Hepes, pH 7.4, 10% FBS, 20 mM L-glutamine, and 1 mM sodium pyruvate immediately before imaging. Cells were imaged by TIRF microscopy on an inverted microscope (Ti-200) as above, using 10 ms of exposure at 488-nm excitation and 10% laser power. Images were captured at 1-s intervals for 5 min, maintaining cells at 37°C using a heated stage (Ibidi). GFP-EB1 comets were tracked using plusTipTracker uTrack version 2.1.3 software (Applegate et al., 2011), and comet velocities, lifetimes, and dynamicity were calculated in MATLAB (version R2015a).

FA disassembly and turnover dynamics

To test the effects of APC silencing and rescue on FA turnover, U2OS cells were transfected with si-oligos or with FL-APC (WT or m4) rescue plasmids and then fixed and immunostained for phospho-Paxillin, FAK-pY397, vinculin, or tubulin. For live imaging of FA translocation (Fig. 4 H), cells were additionally transfected with 600 ng of plasmid expressing GFP-Paxillin in 6-well plates. 48 h after transfection, cells were resuspended in serum-free media for 1 h and then replated for 1 h on collagen-coated glass-bottom dishes. Immediately before imaging, the medium was replaced with serum-free media supplemented with 20 mM Hepes, pH 7.4, and 20 mM L-glutamine. Cells were then imaged by TIRF microscopy, with images captured at 2-s intervals for 30 min (20-ms exposure at 488-nm excitation and 10% laser power), maintaining cells at 37°C in a heated stage (Ibidi). To assess FA disassembly (Fig. 5 A), transfected cells were grown on collagen-coated glass coverslips and then treated with 10 µM nocodazole for 3 h to depolymerize MTs. The drug was washed out with serum-free medium to allow MTs to repolymerize, and at 30-min intervals, cells were fixed in 4% paraformaldehyde in PBS for 15 min at room temperature, processed for immunostaining, and stained for phospho-Paxillin and tubulin. Cells were imaged on an inverted eclipse microscope (Ti-E-PFS3) as above at room temperature. Maximum intensity projections were generated, individual cells were cropped (n = 20 per condition), and the integrated fluorescence intensity of each FA (>1,500 per condition) was quantified in an automated fashion using a custom script in ImageJ. To assess FA levels on Western blots (Fig. 5 C), transfected U2OS cells were grown on 6-well collagen-coated plastic plates, starved with serum-free medium for 12 h, and then treated with 10 µM nocodazole for 3 h. After washing out the drug with serum-free medium, cells were collected at 30-min intervals before preparing whole cell extracts for immunoblotting with antibodies for phospho-Paxillin, total Paxillin, FAK-pY397, and tubulin (see the Western blotting section).

Statistical analysis

All experiments were repeated at least three times, and in each case the data were pooled and averaged, and standard deviations were calculated using Excel 2017 (version 15.32; Microsoft) or Prism (version 6.0c). Figure legends list the n values and error bars (SD or SEM) for each experiment. To test for statistical difference between entire datasets, a one-way ANOVA Bonferroni multiple comparison correction test was used for Fig. 2 (H and J) and Fig. S3 B. A one-way ANOVA Holm-Sidak's multiple comparison test was used for Fig. 2 (D and F),

Fig. 3 (B and C), Fig. 4 E, Fig 5 (B and E), and Fig. S3 (C and F). A one-way Dunnett's multiple comparisons test was used for Figs. 1 D and S1 B. In all other cases, a two-tailed Student's *t* test was performed using Prism (version 6.0c). Statistical tests for colocalization in cells were performed using Mander's correlation coefficient M1 and M2 (with or without threshold) with the Coloc2 plugin in Fiji (version 2.0.0-rc-43/1.51h; Dunn et al., 2011; McDonald and Dunn, 2013). P-values <0.05 were reported as *; p-values <0.01 were reported as **; p-values <0.001 were reported as ***; p-values <0.0001 were reported as ****. Data distribution was assumed to be normal, but this was not formally tested for the individual experiments.

Online supplemental material

Fig. S1 shows mapping actin nucleation activity in the APC Basic domain. Fig. S2 shows biochemical characterization of the APC-B (m4) mutant. Fig. S3 shows the effects of APC silencing and expression of untagged FL-APC (WT) and FL-APC (m4) on MT dynamics, cell migration, and FA turnover. Video 1 shows in vitro TIRF microscopy of APC-B (WT or m4) proteins. Video 2 shows TIRF live-cell imaging and tracking of GFP-EB1 comets in control, si-APC, and FL-APC (WT or m4) rescue U2OS cells. Video 3 shows time-lapse imaging of wound-healing assays of control, si-APC, and FL-APC (WT or m4) rescue U2OS cells. Video 4 shows time-lapse imaging of wound-healing assays of control, si-APC, FL-APC (WT or m4) rescue, and ectopically expressed constructs in U2OS cells. Video 5 shows chemotaxis response to FBS in MDA-MD-231 cells.

Acknowledgments

We are grateful to J. Gelles, G. Gundersen, J. Henty-Ridilla, D. Hilton, S. Jansen, I. Kaverina, A. Johnston, A. Rodal, and S. Shekhar for guidance during the project and feedback on the manuscript, and to L. N'guyen, S. Alioto, S. Del Signore, and S. Wang for technical assistance. We are grateful to A. Barth for providing the GFP-APC plasmid and D. Kast and R. Dominguez for providing the GFP-actin plasmid.

This work was supported by a grant from the National Institutes of Health (GM098143) to B.L. Goode.

The authors declare no competing financial interests.

Author contributions: M.A. Juanes and B.L. Goode conceived of this study; M.A Juanes, H. Bouguenina, and R. Jaiswal performed the experiments; M.A. Juanes and H. Bouguenina, A. Badache, and J.A. Eskin analyzed the data; and M.A Juanes and B.L. Goode wrote the manuscript.

Submitted: 1 February 2017
Revised: 14 April 2017
Accepted: 25 May 2017

References

Akiyama, T., and Y. Kawasaki. 2006. Wnt signalling and the actin cytoskeleton. *Oncogene.* 25:7538–7544. http://dx.doi.org/10.1038/sj.onc.1210063

Amatruda, J.F., and J.A. Cooper. 1992. Purification, characterization, and immunofluorescence localization of Saccharomyces cerevisiae capping protein. *J. Cell Biol.* 117:1067–1076. http://dx.doi.org/10.1083/jcb.117.5.1067

Applegate, K.T., S. Besson, A. Matov, M.H. Bagonis, K. Jaqaman, and G. Danuser. 2011. plusTipTracker: Quantitative image analysis software for the measurement of microtubule dynamics. *J. Struct. Biol.* 176:168–184. http://dx.doi.org/10.1016/j.jsb.2011.07.009

Ballestrem, C., N. Magid, J. Zonis, M. Shtutman, and A. Bershadsky. 2004. Interplay between the actin cytoskeleton, focal adhesions and microtubules. *In* Cell Motility: From Molecules to Organisms. A. Ridley, M. Peckham, and P. Clark, editors. John Wiley & Sons Inc., Chichester, UK. 75–99. http://dx.doi.org/10.1002/0470011742.ch5

Barth, A.I.M., H.Y. Caro-Gonzalez, and W.J. Nelson. 2008. Role of adenomatous polyposis coli (APC) and microtubules in directional cell migration and neuronal polarization. *Semin. Cell Dev. Biol.* 19:245–251. http://dx.doi.org/10.1016/j.semcdb.2008.02.003

Bershadsky, A., A. Chausovsky, E. Becker, A. Lyubimova, and B. Geiger. 1996. Involvement of microtubules in the control of adhesion-dependent signal transduction. *Curr. Biol.* 6:1279–1289. http://dx.doi.org/10.1016/S0960-9822(02)70714-8

Bouchet, B.P., R.E. Gough, Y.-C. Ammon, D. van de Willige, H. Post, G. Jacquemet, A.M. Altelaar, A.J. Heck, B.T. Goult, and A. Akhmanova. 2016. Talin-KANK1 interaction controls the recruitment of cortical microtubule stabilizing complexes to focal adhesions. *eLife.* 5. http://dx.doi.org/10.7554/eLife.18124

Bravo-Cordero, J.J., L. Hodgson, and J. Condeelis. 2012. Directed cell invasion and migration during metastasis. *Curr. Opin. Cell Biol.* 24:277–283. http://dx.doi.org/10.1016/j.ceb.2011.12.004

Breitsprecher, D., and B.L. Goode. 2013. Formins at a glance. *J. Cell Sci.* 126:1–7. http://dx.doi.org/10.1242/jcs.107250

Breitsprecher, D., R. Jaiswal, J.P. Bombardier, C.J. Gould, J. Gelles, and B.L. Goode. 2012. Rocket launcher mechanism of collaborative actin assembly defined by single-molecule imaging. *Science.* 336:1164–1168. http://dx.doi.org/10.1126/science.1218062

Castoldi, M., and A.V. Popov. 2003. Purification of brain tubulin through two cycles of polymerization-depolymerization in a high-molarity buffer. *Protein Expr. Purif.* 32:83–88. http://dx.doi.org/10.1016/S1046-5928(03)00218-3

Chao, W.-T., and J. Kunz. 2009. Focal adhesion disassembly requires clathrin-dependent endocytosis of integrins. *FEBS Lett.* 583:1337–1343. http://dx.doi.org/10.1016/j.febslet.2009.03.037

Chao, W.-T., F. Ashcroft, A.C. Daquinag, T. Vadakkan, Z. Wei, P. Zhang, M.E. Dickinson, and J. Kunz. 2010. Type I phosphatidylinositol phosphate kinase beta regulates focal adhesion disassembly by promoting β1 integrin endocytosis. *Mol. Cell. Biol.* 30:4463–4479. http://dx.doi.org/10.1128/MCB.01207-09

Cooper, J.A., J.D. Blum, and T.D. Pollard. 1984. Acanthamoeba castellanii capping protein: properties, mechanism of action, immunologic cross-reactivity, and localization. *J. Cell Biol.* 99:217–225. http://dx.doi.org/10.1083/jcb.99.1.217

Daou, P., S. Hasan, D. Breitsprecher, E. Baudelet, L. Camoin, S. Audebert, B.L. Goode, and A. Badache. 2014. Essential and nonredundant roles for Diaphanous formins in cortical microtubule capture and directed cell migration. *Mol. Biol. Cell.* 25:658–668. http://dx.doi.org/10.1091/mbc.E13-08-0482

Dunn, K.W., M.M. Kamocka, and J.H. McDonald. 2011. A practical guide to evaluating colocalization in biological microscopy. *Am. J. Physiol. Cell Physiol.* 300:C723–C742. http://dx.doi.org/10.1152/ajpcell.00462.2010

Efimov, A., N. Schiefermeier, I. Grigoriev, R. Ohi, M.C. Brown, C.E. Turner, J.V. Small, and I. Kaverina. 2008. Paxillin-dependent stimulation of microtubule catastrophes at focal adhesion sites. *J. Cell Sci.* 121:196–204. http://dx.doi.org/10.1242/jcs.012666

Ezratty, E.J., M.A. Partridge, and G.G. Gundersen. 2005. Microtubule-induced focal adhesion disassembly is mediated by dynamin and focal adhesion kinase. *Nat. Cell Biol.* 7:581–590. http://dx.doi.org/10.1038/ncb1262

Ezratty, E.J., C. Bertaux, E.E. Marcantonio, and G.G. Gundersen. 2009. Clathrin mediates integrin endocytosis for focal adhesion disassembly in migrating cells. *J. Cell Biol.* 187:733–747. http://dx.doi.org/10.1083/jcb.200904054

Foxman, E.F., E.J. Kunkel, and E.C. Butcher. 1999. Integrating conflicting chemotactic signals. The role of memory in leukocyte navigation. *J. Cell Biol.* 147:577–588. http://dx.doi.org/10.1083/jcb.147.3.577

Goode, B.L., J.J. Wong, A.C. Butty, M. Peter, A.L. McCormack, J.R. Yates, D.G. Drubin, and G. Barnes. 1999. Coronin promotes the rapid assembly and cross-linking of actin filaments and may link the actin and microtubule cytoskeletons in yeast. *J. Cell Biol.* 144:83–98. http://dx.doi.org/10.1083/jcb.144.1.83

Henty-Ridilla, J.L., A. Rankova, J.A. Eskin, K. Kenny, and B.L. Goode. 2016. Accelerated actin filament polymerization from microtubule plus ends. *Science.* 352:1004–1009. http://dx.doi.org/10.1126/science.aaf1709

Jaiswal, R., D. Breitsprecher, A. Collins, I.R. Corrêa Jr., M.-Q. Xu, and B.L. Goode. 2013a. The formin Daam1 and fascin directly collaborate to promote filopodia formation. *Curr. Biol.* 23:1373–1379. http://dx.doi.org/10.1016/j.cub.2013.06.013

Jaiswal, R., V. Stepanik, A. Rankova, O. Molinar, B.L. Goode, and B.M. McCartney. 2013b. *Drosophila* homologues of adenomatous polyposis coli (APC) and the formin diaphanous collaborate by a conserved mechanism to stimulate actin filament assembly. *J. Biol. Chem.* 288:13897–13905. http://dx.doi.org/10.1074/jbc.M113.462051

Joslyn, G., D.S. Richardson, R. White, and T. Alber. 1993. Dimer formation by an N-terminal coiled coil in the APC protein. *Proc. Natl. Acad. Sci. USA.* 90:11109–11113. http://dx.doi.org/10.1073/pnas.90.23.11109

Kaverina, I., K. Rottner, and J.V. Small. 1998. Targeting, capture, and stabilization of microtubules at early focal adhesions. *J. Cell Biol.* 142:181–190. http://dx.doi.org/10.1083/jcb.142.1.181

Kaverina, I., O. Krylyshkina, and J.V. Small. 1999. Microtubule targeting of substrate contacts promotes their relaxation and dissociation. *J. Cell Biol.* 146:1033–1044. http://dx.doi.org/10.1083/jcb.146.5.1033

Kenific, C.M., S.J. Stehbens, J. Goldsmith, A.M. Leidal, N. Faure, J. Ye, T. Wittmann, and J. Debnath. 2016. NBR1 enables autophagy-dependent focal adhesion turnover. *J. Cell Biol.* 212:577–590. http://dx.doi.org/10.1083/jcb.201503075

Kinzler, K.W., M.C. Nilbert, L.K. Su, B. Vogelstein, T.M. Bryan, D.B. Levy, K.J. Smith, A.C. Preisinger, P. Hedge, D. McKechnie, et al. 1991. Identification of FAP locus genes from chromosome 5q21. *Science.* 253:661–665. http://dx.doi.org/10.1126/science.1651562

Kirchner, J., Z. Kam, G. Tzur, A.D. Bershadsky, and B. Geiger. 2003. Live-cell monitoring of tyrosine phosphorylation in focal adhesions following microtubule disruption. *J. Cell Sci.* 116:975–986. http://dx.doi.org/10.1242/jcs.00284

Kovar, D.R., E.S. Harris, R. Mahaffy, H.N. Higgs, and T.D. Pollard. 2006. Control of the assembly of ATP- and ADP-actin by formins and profilin. *Cell.* 124:423–435. http://dx.doi.org/10.1016/j.cell.2005.11.038

Kroboth, K., I.P. Newton, K. Kita, D. Dikovskaya, J. Zumbrunn, C.M. Waterman-Storer, and I.S. Näthke. 2007. Lack of adenomatous polyposis coli protein correlates with a decrease in cell migration and overall changes in microtubule stability. *Mol. Biol. Cell.* 18:910–918. http://dx.doi.org/10.1091/mbc.E06-03-0179

Krylyshkina, O., I. Kaverina, W. Kranewitter, W. Steffen, M.C. Alonso, R.A. Cross, and J.V. Small. 2002. Modulation of substrate adhesion dynamics via microtubule targeting requires kinesin-1. *J. Cell Biol.* 156:349–359. http://dx.doi.org/10.1083/jcb.200105051

Krylyshkina, O., K.I. Anderson, I. Kaverina, I. Upmann, D.J. Manstein, J.V. Small, and D.K. Toomre. 2003. Nanometer targeting of microtubules to focal adhesions. *J. Cell Biol.* 161:853–859. http://dx.doi.org/10.1083/jcb.200301102

Kuhn, J.R., and T.D. Pollard. 2005. Real-time measurements of actin filament polymerization by total internal reflection fluorescence microscopy. *Biophys. J.* 88:1387–1402. http://dx.doi.org/10.1529/biophysj.104.047399

Kunttas-Tatli, E., D.M. Roberts, and B.M. McCartney. 2014. Self-association of the APC tumor suppressor is required for the assembly, stability, and activity of the Wnt signaling destruction complex. *Mol. Biol. Cell.* 25:3424–3436. http://dx.doi.org/10.1091/mbc.E14-04-0885

Kwong, L.N., and W.F. Dove. 2009. APC and its modifiers in colon cancer. *Adv. Exp. Med. Biol.* 656:85–106. http://dx.doi.org/10.1007/978-1-4419-1145-2_8

Langford, K.J., J.M. Askham, T. Lee, M. Adams, and E.E. Morrison. 2006a. Examination of actin and microtubule dependent APC localisations in living mammalian cells. *BMC Cell Biol.* 7:3. http://dx.doi.org/10.1186/1471-2121-7-3

Langford, K.J., T. Lee, J.M. Askham, and E.E. Morrison. 2006b. Adenomatous polyposis coli localization is both cell type and cell context dependent. *Cell Motil. Cytoskeleton.* 63:483–492. http://dx.doi.org/10.1002/cm.20139

Li, Z., K. Kroboth, I.P. Newton, and I.S. Näthke. 2008. Novel self-association of the APC molecule affects APC clusters and cell migration. *J. Cell Sci.* 121:1916–1925. http://dx.doi.org/10.1242/jcs.029470

Matsumoto, S., K. Fumoto, T. Okamoto, K. Kaibuchi, and A. Kikuchi. 2010. Binding of APC and dishevelled mediates Wnt5a-regulated focal adhesion dynamics in migrating cells. *EMBO J.* 29:1192–1204. http://dx.doi.org/10.1038/emboj.2010.26

McCartney, B.M., and I.S. Näthke. 2008. Cell regulation by the Apc protein: Apc as master regulator of epithelia. *Curr. Opin. Cell Biol.* 20:186–193. http://dx.doi.org/10.1016/j.ceb.2008.02.001

McDonald, J.H., and K.W. Dunn. 2013. Statistical tests for measures of colocalization in biological microscopy. *J. Microsc.* 252:295–302. http://dx.doi.org/10.1111/jmi.12093

Mills, K.M., M.G. Brocardo, and B.R. Henderson. 2016. APC binds the Miro/Milton motor complex to stimulate transport of mitochondria to the plasma membrane. *Mol. Biol. Cell.* 27:466–482. http://dx.doi.org/10.1091/mbc.E15-09-0632

Mimori-Kiyosue, Y., N. Shiina, and S. Tsukita. 2000. Adenomatous polyposis coli (APC) protein moves along microtubules and concentrates at their growing ends in epithelial cells. *J. Cell Biol.* 148:505–518. http://dx.doi.org/10.1083/jcb.148.3.505

Mogensen, M.M., J.B. Tucker, J.B. Mackie, A.R. Prescott, and I.S. Näthke. 2002. The adenomatous polyposis coli protein unambiguously localizes to microtubule plus ends and is involved in establishing parallel arrays of microtubule bundles in highly polarized epithelial cells. *J. Cell Biol.* 157:1041–1048. http://dx.doi.org/10.1083/jcb.200203001

Moseley, J.B., and B.L. Goode. 2005. Differential activities and regulation of *Saccharomyces cerevisiae* formin proteins Bni1 and Bnr1 by Bud6. *J. Biol. Chem.* 280:28023–28033. http://dx.doi.org/10.1074/jbc.M503094200

Moseley, J.B., I. Sagot, A.L. Manning, Y. Xu, M.J. Eck, D. Pellman, and B.L. Goode. 2004. A conserved mechanism for Bni1- and mDia1-induced actin assembly and dual regulation of Bni1 by Bud6 and profilin. *Mol. Biol. Cell.* 15:896–907. http://dx.doi.org/10.1091/mbc.E03-08-0621

Moseley, J.B., F. Bartolini, K. Okada, Y. Wen, G.G. Gundersen, and B.L. Goode. 2007. Regulated binding of adenomatous polyposis coli protein to actin. *J. Biol. Chem.* 282:12661–12668. http://dx.doi.org/10.1074/jbc.M610615200

Munemitsu, S., B. Souza, O. Müller, I. Albert, B. Rubinfeld, and P. Polakis. 1994. The APC gene product associates with microtubules in vivo and promotes their assembly in vitro. *Cancer Res.* 54:3676–3681.

Näthke, I.S. 2004. The adenomatous polyposis coli protein: the Achilles heel of the gut epithelium. *Annu. Rev. Cell Dev. Biol.* 20:337–366. http://dx.doi.org/10.1146/annurev.cellbio.20.012103.094541

Näthke, I. 2005. Relationship between the role of the adenomatous polyposis coli protein in colon cancer and its contribution to cytoskeletal regulation. *Biochem. Soc. Trans.* 33:694–697. http://dx.doi.org/10.1042/BST0330694

Näthke, I.S., C.L. Adams, P. Polakis, J.H. Sellin, and W.J. Nelson. 1996. The adenomatous polyposis coli tumor suppressor protein localizes to plasma membrane sites involved in active cell migration. *J. Cell Biol.* 134:165–179. http://dx.doi.org/10.1083/jcb.134.1.165

Nelson, S., and I.S. Näthke. 2013. Interactions and functions of the adenomatous polyposis coli (APC) protein at a glance. *J. Cell Sci.* 126:873–877. http://dx.doi.org/10.1242/jcs.100479

Okada, K., F. Bartolini, A.M. Deaconescu, J.B. Moseley, Z. Dogic, N. Grigorieff, G.G. Gundersen, and B.L. Goode. 2010. Adenomatous polyposis coli protein nucleates actin assembly and synergizes with the formin mDia1. *J. Cell Biol.* 189:1087–1096. http://dx.doi.org/10.1083/jcb.201001016

Ridley, A.J., M.A. Schwartz, K. Burridge, R.A. Firtel, M.H. Ginsberg, G. Borisy, J.T. Parsons, and A.R. Horwitz. 2003. Cell migration: integrating signals from front to back. *Science.* 302:1704–1709. http://dx.doi.org/10.1126/science.1092053

Rodriguez, O.C., A.W. Schaefer, C.A. Mandato, P. Forscher, W.M. Bement, and C.M. Waterman-Storer. 2003. Conserved microtubule-actin interactions in cell movement and morphogenesis. *Nat. Cell Biol.* 5:599–609. http://dx.doi.org/10.1038/ncb0703-599

Rosin-Arbesfeld, R., G. Ihrke, and M. Bienz. 2001. Actin-dependent membrane association of the APC tumour suppressor in polarized mammalian epithelial cells. *EMBO J.* 20:5929–5939. http://dx.doi.org/10.1093/emboj/20.21.5929

Ruane, P.T., L.F. Gumy, B. Bola, B. Anderson, M.J. Wozniak, C.C. Hoogenraad, and V.J. Allan. 2016. Tumour Suppressor Adenomatous Polyposis Coli (APC) localisation is regulated by both Kinesin-1 and Kinesin-2. *Sci. Rep.* 6. http://dx.doi.org/10.1038/srep27456

Sansom, O.J., K.R. Reed, A.J. Hayes, H. Ireland, H. Brinkmann, I.P. Newton, E. Batlle, P. Simon-Assmann, H. Clevers, I.S. Nathke, et al. 2004. Loss of Apc in vivo immediately perturbs Wnt signaling, differentiation, and migration. *Genes Dev.* 18:1385–1390. http://dx.doi.org/10.1101/gad.287404

Shaw, T.J., and P. Martin. 2016. Wound repair: a showcase for cell plasticity and migration. *Curr. Opin. Cell Biol.* 42:29–37. http://dx.doi.org/10.1016/j.ceb.2016.04.001

Small, J.V., B. Geiger, I. Kaverina, and A. Bershadsky. 2002. How do microtubules guide migrating cells? *Nat. Rev. Mol. Cell Biol.* 3:957–964. http://dx.doi.org/10.1038/nrm971

Smilenov, L.B., A. Mikhailov, R.J. Pelham, E.E. Marcantonio, and G.G. Gundersen. 1999. Focal adhesion motility revealed in stationary fibroblasts. *Science.* 286:1172–1174. http://dx.doi.org/10.1126/science.286.5442.1172

Soeno, Y., H. Abe, S. Kimura, K. Maruyama, and T. Obinata. 1998. Generation of functional β-actinin (CapZ) in an *E. coli* expression system. *J. Muscle Res. Cell Motil.* 19:639–646. http://dx.doi.org/10.1023/A:1005329114263

Spudich, J.A., and S. Watt. 1971. The regulation of rabbit skeletal muscle contraction. I. Biochemical studies of the interaction of the tropomyosin-troponin complex with actin and the proteolytic fragments of myosin. *J. Biol. Chem.* 246:4866–4871.

Stehbens, S., and T. Wittmann. 2012. Targeting and transport: how microtubules control focal adhesion dynamics. *J. Cell Biol.* 198:481–489. http://dx.doi.org/10.1083/jcb.201206050

Stehbens, S.J., M. Paszek, H. Pemble, A. Ettinger, S. Gierke, and T. Wittmann. 2014. CLASPs link focal-adhesion-associated microtubule capture to localized exocytosis and adhesion site turnover. *Nat. Cell Biol.* 16:561–573. http://dx.doi.org/10.1038/ncb2975

Su, L.K., B. Vogelstein, and K.W. Kinzler. 1993. Association of the APC tumor suppressor protein with catenins. *Science.* 262:1734–1737. http://dx.doi.org/10.1126/science.8259519

Watanabe, T., S. Wang, J. Noritake, K. Sato, M. Fukata, M. Takefuji, M. Nakagawa, N. Izumi, T. Akiyama, and K. Kaibuchi. 2004. Interaction with IQGAP1 links APC to Rac1, Cdc42, and actin filaments during cell polarization and migration. *Dev. Cell.* 7:871–883. http://dx.doi.org/10.1016/j.devcel.2004.10.017

Webb, D.J., J.T. Parsons, and A.F. Horwitz. 2002. Adhesion assembly, disassembly and turnover in migrating cells -- over and over and over again. *Nat. Cell Biol.* 4:E97–E100. http://dx.doi.org/10.1038/ncb0402-e97

Webb, R.L., M.-N. Zhou, and B.M. McCartney. 2009. A novel role for an APC2-Diaphanous complex in regulating actin organization in *Drosophila*. *Development.* 136:1283–1293. http://dx.doi.org/10.1242/dev.026963

Weijer, C.J. 2009. Collective cell migration in development. *J. Cell Sci.* 122:3215–3223. http://dx.doi.org/10.1242/jcs.036517

Wu, X., A. Kodama, and E. Fuchs. 2008. ACF7 regulates cytoskeletal-focal adhesion dynamics and migration and has ATPase activity. *Cell.* 135:137–148. http://dx.doi.org/10.1016/j.cell.2008.07.045

Yue, J., Y. Zhang, W.G. Liang, X. Gou, P. Lee, H. Liu, W. Lyu, W.-J. Tang, S.-Y. Chen, F. Yang, et al. 2016. In vivo epidermal migration requires focal adhesion targeting of ACF7. *Nat. Commun.* 7. http://dx.doi.org/10.1038/ncomms11692

Zaidel-Bar, R., S. Itzkovitz, A. Ma'ayan, R. Iyengar, and B. Geiger. 2007. Functional atlas of the integrin adhesome. *Nat. Cell Biol.* 9:858–867. http://dx.doi.org/10.1038/ncb0807-858

Zaoui, K., S. Honoré, D. Isnardon, D. Braguer, and A. Badache. 2008. Memo-RhoA-mDia1 signaling controls microtubules, the actin network, and adhesion site formation in migrating cells. *J. Cell Biol.* 183:401–408. http://dx.doi.org/10.1083/jcb.200805107

Zaoui, K., K. Benseddik, P. Daou, D. Salaün, and A. Badache. 2010. ErbB2 receptor controls microtubule capture by recruiting ACF7 to the plasma membrane of migrating cells. *Proc. Natl. Acad. Sci. USA.* 107:18517–18522. http://dx.doi.org/10.1073/pnas.1000975107

Zhou, M.-N., E. Kunttas-Tatli, S. Zimmerman, F. Zhouzheng, and B.M. McCartney. 2011. Cortical localization of APC2 plays a role in actin organization but not in Wnt signaling in *Drosophila*. *J. Cell Sci.* 124:1589–1600. http://dx.doi.org/10.1242/jcs.073916